

## Geochemistry, Geophysics, Geosystems

### RESEARCH ARTICLE

10.1002/2016GC006667

#### Special Section:

The Lithosphere-  
asthenosphere System

#### Key Points:

- LAB topography varies between ~85 and 145 km depth
- A thin lithosphere is associated with a zone of anomalous conductivity
- The lithospheric anomalous conductivity zone (LACZ) possibly results from kimberlite intrusions or alteration in rheology due to localized rift-related deformation

#### Correspondence to:

E. Attias,  
eric.attias@noc.soton.ac.uk

#### Citation:

Attias, E., R. L. Evans, S. Naif, J. Elsenbeck, and K. Key (2017), Conductivity structure of the lithosphere-asthenosphere boundary beneath the eastern North American margin, *Geochim. Geophys. Geosyst.*, 18, 676–696, doi:10.1002/2016GC006667.

Received 3 OCT 2016

Accepted 18 JAN 2017

Accepted article online 31 JAN 2017

Published online 25 FEB 2017

### Conductivity structure of the lithosphere-asthenosphere boundary beneath the eastern North American margin

Eric Attias<sup>1</sup> , Rob. L. Evans<sup>2</sup> , Samer Naif<sup>3</sup> , Jimmy Elsenbeck<sup>2</sup> , and Kerry Key<sup>3</sup> 

<sup>1</sup>Ocean and Earth Science, National Oceanography Centre Southampton, University of Southampton, European Way, Southampton, UK, <sup>2</sup>Department of Geology and Geophysics, Woods Hole Oceanographic Institution, Woods Hole, Massachusetts, USA, <sup>3</sup>Lamont Doherty Earth Observatory, Columbia University, Palisades, New York, USA

**Abstract** Tectonic plate motion and mantle dynamics processes are heavily influenced by the characteristics of the lithosphere-asthenosphere boundary (LAB), yet this boundary remains enigmatic regarding its properties and geometry. The processes involved in rifting at passive margins result in substantial alteration of the lithosphere through the transition from continental to oceanic lithologies. Here we employ marine magnetotelluric (MT) data acquired along a ~135 km long profile, offshore Martha's Vineyard, New England, USA, to image the electrical conductivity structure beneath the New England continental margin for the first time. We invert the data using two different MT 2-D inversion algorithms and present a series of models that are obtained using three different parameterizations: fully unconstrained, unconstrained with an imposed LAB discontinuity and a priori constrained lithosphere resistivity. This suite of models infers variability in the depth of the LAB, with an average depth of 115 km at the eastern North America passive margin. Models robustly detect a ~350  $\Omega\text{m}$  lithospheric anomalous conductivity zone (LACZ) that extends vertically through the entire lithosphere. Our preferred conductivity model is consistent with regional *P*-to-*S* receiver function data, shear-wave velocity, gravity anomalies, and prominent geological features. We propose that the LACZ is indicative of paleolithospheric thinning, either resulting from kimberlite intrusions associated with rifting and the New England Great Meteor hot spot track, or from shear-driven localized deformation related to rifting.

### 1. Introduction

The Earth's *lithosphere* is a rigid mechanical boundary that is underlain by a weaker convecting *asthenosphere*. The sharpness of transition at the lithosphere-asthenosphere boundary (LAB) is widely debated [e.g., Eaton *et al.*, 2009]. In this framework, rheological alterations across the LAB are manifested by a separation of the overlying lithospheric plate from the underlying convecting mantle. This boundary may exhibit localized deformation [Eaton *et al.*, 2009; Höink *et al.*, 2012], which may result in electrical and seismic anomalies [Kawakatsu *et al.*, 2009; Naif *et al.*, 2013]. Tectonic plate motion and mantle dynamics are inherently governed by the characteristics of the LAB. Rheological differences within the LAB can be detected using a variety of geophysical methods, such as seismic velocities, electrical conductivity, and heat flow regime. Yet, significant uncertainty and ambiguity exist regarding the depth and sharpness of the LAB and the rheological contrast between the lithosphere and asthenosphere [Fischer *et al.*, 2010].

Global surface shear-wave tomography studies suggest that young oceanic crust encompasses a thin lithosphere, in contrast to an old oceanic crust and continental cratons which exhibit much thicker and higher velocity lithosphere [e.g., Cammarano and Romanowicz, 2007; Kustowski *et al.*, 2008; Lebedev and Van Der Hilst, 2008; Dalton *et al.*, 2009; Romanowicz, 2009]. Across the LAB, a purely thermal transition from cold lithosphere to warm asthenosphere produces a decrease in seismic velocity, whereas the presence of partial melt or a dehydration boundary in the asthenosphere can dramatically increase the velocity contrast [e.g., Hammond and Humphreys, 2000; Kawakatsu *et al.*, 2009; Artemieva, 2009]. Commonly, regions with a lithosphere thicker than 150 km will produce a gradual LAB, while areas with a thin lithosphere <120 km exhibit a sharper transition [Abt *et al.*, 2010].

LAB discontinuities are found at depths ranging from 50 to 130 km beneath oceanic regions [e.g., Li *et al.*, 2004; Kumar *et al.*, 2005; Kawakatsu *et al.*, 2009; Rychert and Shearer, 2009], and below relatively thin continental lithosphere [e.g., Rychert *et al.*, 2007; Li *et al.*, 2007; Rychert and Shearer, 2009]. Beneath cratons,

shear-wave receiver function studies revealed deeper LAB discontinuities ranging between 130 and 300 km depth [e.g., Mohsen *et al.*, 2006; Wittlinger and Farra, 2007; Snyder, 2008; Hansen *et al.*, 2009].

The eastern North American continental rift margin is characterized by significant seismic velocity heterogeneities [e.g., Levin *et al.*, 2000; Chu *et al.*, 2013; Schmandt and Lin, 2014; Pollitz and Mooney, 2016]. At this continental rift margin, a full waveform tomography study indicates that the lithosphere is successively broken into relatively thin (100–150 km) high-velocity blocks that extend about 200–300 km horizontally into the Atlantic Ocean [Yuan *et al.*, 2014]. A receiver function study in this region detected sharp velocity reductions of 5–10% within a 5–11 km vertical distance across the LAB at depths of 87–105 km [Rychert *et al.*, 2007].

Geophysical studies frequently use the magnetotelluric (MT) method to image the conductivity structure of the lithosphere and the upper mantle, both in continental [e.g., Singh *et al.*, 1995; Wannamaker *et al.*, 1996; Fullea *et al.*, 2011; Vozar *et al.*, 2014; Yang *et al.*, 2015] and oceanic regions [e.g., Cox, 1981; Lizarralde *et al.*, 1995; Evans *et al.*, 1999; Baba *et al.*, 2013; Key *et al.*, 2013; Sarafian *et al.*, 2015]. Cold oceanic lithosphere typically exhibits high resistivity values of  $10^3$ – $10^5$   $\Omega\text{m}$  [e.g., Cox *et al.*, 1986; Evans *et al.*, 2005; Kapinos *et al.*, 2016], whereas the resistivity of the warm upper mantle at greater depths is reduced to 10–100  $\Omega\text{m}$  [e.g., Baba *et al.*, 2006; Naif *et al.*, 2013; Key *et al.*, 2013; Sarafian *et al.*, 2015].

Electromagnetic observations are sensitive to the presence of water dissolved in mantle minerals as well as connected networks of partial melt [e.g., Evans, 2012]. Thus, highly conductive upper mantle may indicate a rheological contrast across the LAB [e.g., Naif *et al.*, 2013]. The depth at which high conductivity structures appear varies substantially depending on the tectonic setting. For example, high conductivities of less than 10  $\Omega\text{m}$  are observed at depths greater than 20 km beneath the ridge axis of the northern East Pacific Rise [Key *et al.*, 2013], compared with depths greater than 45–80 km beneath the Cocos oceanic plate adjacent to a subduction zone [Worzewski *et al.*, 2011; Naif *et al.*, 2013]. A long period EarthScope MT study in Central North USA suggests that the LAB is at  $\sim$ 200 km depth, where the resistivity drops below  $\sim$ 100  $\Omega\text{m}$  [Yang *et al.*, 2015]. At the Superior-Grenville margin, a relatively sharp resistivity contrast (from  $\sim$ 100  $\Omega\text{m}$  to less than  $\sim$ 20  $\Omega\text{m}$ ) indicates that the LAB is located at a depth of 160 km [Adetunji *et al.*, 2014].

Here we present the results of the first MT study conducted with the aim to reveal the depth and topography of the LAB along the eastern North America passive continental margin, nearshore of Martha's Vineyard, Massachusetts, USA (Figure 1). The 2-D conductivity structure of the lithosphere and asthenosphere was resolved using two different inversion methods. We interpret our preferred 2-D conductivity model on a broader regional scale while considering additional geophysical information from *P*-to-*S* receiver function data, shear-wave velocity models, and a localized gravity anomaly, evaluated in conjunction with regional geological features.

## 2. Geologic Setting

The continental margin of eastern North America is defined as a passive margin that evolved from rifting during the breakup of Pangea and the opening of the Atlantic in the Late Triassic to Early Jurassic. Most rift basins in this region are asymmetric, with a strike of  $\sim$ 45°, and bounded by a series of normal faults [Withjack *et al.*, 1998; Yuan *et al.*, 2014]. These boundary faults are reactivated pre-existing structures that reflect the crustal fabric produced during the Paleozoic orogenies [e.g., Ratcliffe and Burton, 1985; Olsen *et al.*, 1989; de Voogd *et al.*, 1990]. During the late Triassic and early Jurassic, the northeastern rift basins were filled by evaporites such as halite and carbonate. During the late Jurassic and Early Cretaceous, shallow marine sandstones and mudstones filled the northern segment of these rift basins [e.g., McAlpine, 1990]. Subsidence patterns in eastern North America varied spatially and temporally during rifting. The thickness of the Upper Triassic synrift rocks within the eastern North American rift system is less than in the southern and central segments [e.g., Tseng *et al.*, 1996; Malinconico, 2003]. Thus, extension rates were greater in the south during the Late Triassic.

Igneous activity that occurred during the earliest Jurassic resulted in the Central Atlantic Magmatic Province (CAMP), which included basalts, dikes, and intrusive sheets [e.g., McHone, 1996; Marzoli *et al.*, 1999]. In the central segment of the eastern North American rift system, CAMP related basalt flows are within the synrift, providing evidence that the CAMP activity occurred mainly during rifting. Dike trends suggest that extension occurred from NW to SE during CAMP magmatic activity in the central and northern segments. During

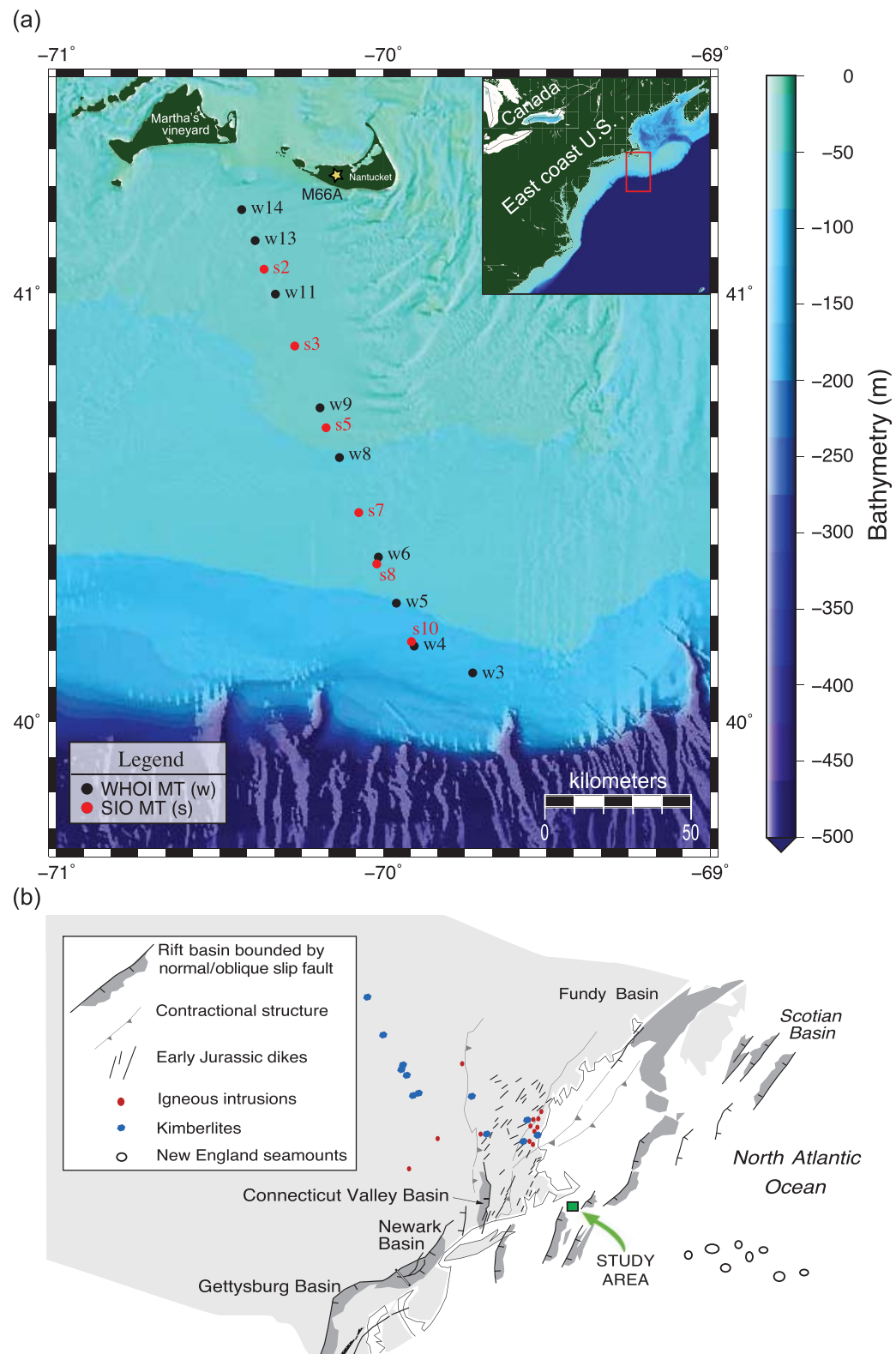


**Figure 1.** Study area local and regional maps. (a) The survey linear array consists of MT station from WHOI and SIO. The map insert shows the survey region along the east coast of the United States. The star in Nantucket Island denotes the position of a teleseismic receiver (M66A) that is used for receiver function analysis [Rondenay et al., 2017]. (b) Key geological features at the vicinity of the study area, marked by a green square (map modified from Crough [1981], Withjack et al. [1998], and Eaton and Frederiksen [2007]).

the mid-Jurassic, the basins in the northern segment continued to widen and deepen in response to continued rifting. In the late Jurassic and early Cretaceous, subsidence rates increased significantly in the northern segment of the eastern North American rift system, reflecting renewed or accelerated extension [e.g., *Withjack et al.*, 1995; *Olsen et al.*, 1996; *Welsink et al.*, 1989].

In addition to CAMP volcanics, another large igneous province is present beneath the US East coast continental margin, with a volume estimated to be as much as  $2.7 \times 10^6 \text{ km}^3$  [*Kelemen and Holbrook*, 1995]. The formation of this igneous province occurred during the transition from rifting to seafloor spreading near the continent-ocean boundary [e.g., *Holbrook and Kelemen*, 1993; *Sheridan et al.*, 1993; *Kelemen and Holbrook*, 1995]. After the breakup of Pangea, the eastern US margin subsided and accumulated large amounts of sediments that overlay the Jurassic basement [e.g., *Schlee et al.*, 1976; *Poag*, 1978; *Hutchinson et al.*, 1986; *Manspeizer and Cousminer*, 1988; *Olsen et al.*, 1989; *Steckler et al.*, 1999]. Early Jurassic ( $\sim 200 \text{ Ma}$ ) basaltic volcanism was responsible for the intrusion of diabase dikes (Figure 1b) and sills along with extrusion of basalt flows throughout eastern North America [e.g., *Olsen et al.*, 1989; *McHone*, 1996; *Hames et al.*, 2000]. Seaward-dipping reflections along the US Atlantic continental margin have been interpreted as a wedge consisting of Jurassic volcanic rocks [*Benson and Doyle*, 1988; *Austin et al.*, 1990].

Along the New England continental margin, asthenospheric upwelling during the Triassic/Jurassic rifting exceeded the lithospheric spreading rate. Consequently, 25 km of mafic igneous crust accumulated over  $>1000 \text{ km}$  along the strike of the margin [e.g., *Holbrook and Kelemen*, 1993; *Sheridan et al.*, 1993; *Holbrook et al.*, 1994]. Along this margin, basaltic magmatism and rifting are attributed to convection cells beneath the rift zones [*McHone*, 2000] rather than a mantle plume mechanism [e.g., *Holbrook and Kelemen*, 1993; *Holbrook et al.*, 1994; *Bédard*, 1985; *McHone*, 2000]. For example, the Northern Appalachian Anomaly (NAA), a distinctive shear velocity contrast ( $\sim 10\%$ ) which appears as a low velocity in the upper mantle at 200 km depth beneath southern New England, is interpreted to be caused by small-scale upwelling from an eddy in the asthenospheric flow field at the New England continental margin [*Menke et al.*, 2016].

The New England Seamounts (Figure 1b) are related to the Great Meteor hot spot track [e.g., *Morgan*, 1981, 1983; *Duncan*, 1984; *Sleep*, 1990]. The magmatic activity that created the seamount chain along an extension of transverse Appalachian fracture zones [e.g., *Crough*, 1981; *McHone and Butler*, 1984; *Olsen et al.*, 1989; *Dunning and Hodych*, 1990], is thought to be unrelated to the magmatism associated with the rift zone. In Mesozoic time, the northwestward movement of North America over the Great Meteor hot spot created an elongated topographic swell, which led to substantial uplift and erosion along the hot spot axis [*Crough et al.*, 1980; *Crough*, 1981]. The axis of this uplift cross-cuts the New England coastline and the Appalachian trend parallel to the Great Meteor hot spot track [*Crough*, 1981]. At the East-central USA, the lithosphere is thought to have thickened from 70 km at the end of the Appalachian orogeny to 150 km thick at present as the plate moved NNW [*Deschamps et al.*, 2008].

Intraplate magmatism produced by mantle hot spots can generate a wide variety of landforms and intrusive igneous rocks [*Crough et al.*, 1980; *Kamara*, 1981; *Kjarsgaard*, 2007]. Hot spot tracks are usually observed on oceanic or thin continental lithosphere, whereas in thick continental lithosphere (e.g., the eastern USA) such tracks are deduced from sporadic kimberlite intrusions, generally sourced from deep mantle [*Crough et al.*, 1980; *Torsvik et al.*, 2010; *Chu et al.*, 2013]. Hot spot driven kimberlite eruptions can pierce the lithosphere from depths  $>150 \text{ km}$  to the surface, providing information on melting processes and the composition of the deep subcontinental mantle lithosphere [*Heaman and Kjarsgaard*, 2000; *Torsvik et al.*, 2010]. Within eastern North America, kimberlite intrusions form mainly within  $5^\circ$  of a mantle hot spot [*Crough et al.*, 1980]. These kimberlite intrusions strongly support the notion that mantle melting occurred  $\sim 140\text{--}200 \text{ Ma}$  along the Great Meteor hot spot track [*Crough et al.*, 1980; *Heaman and Kjarsgaard*, 2000; *Eaton and Frederiksen*, 2007; *Selway*, 2014]. This hot spot track is misaligned with respect to its location at 200 km depth, projected westward from the surface possibly due to asthenospheric flow that deformed the lithospheric keel [*Eaton and Frederiksen*, 2007].

### 3. Methods

#### 3.1. Data Acquisition and Processing

To image the electrical conductivity structure across the eastern North America continental shelf, a linear array of MT instruments owned by the Woods Hole Oceanographic Institution (WHOI) and by Scripps

Institution of Oceanography (SIO) were deployed in August 2013 (WHOI) and 2015 (SIO) (Figure 1a). The WHOI MT instruments are long period with fluxgate magnetometers whereas the SIO MT instruments are broadband with induction coils [Constable *et al.*, 1998]. The profile is ~135 km long, aligned from NNW to SSE and oriented at approximately 120° to the regional rift basins (Figure 1b), which are bounded by normal and oblique-slip faults [e.g., Manspeizer and Cousminer, 1988; Olsen *et al.*, 1989; Withjack *et al.*, 1998]. Site spacing varied between 1 and 15 km, with the majority of the stations spaced ~10 km apart. The instruments were deployed from a vessel and allowed to free fall into position. Water depths of sites ranged between 33 and 103 m, over smooth gently sloping bathymetry. Other than the coastlines to the north and the continental shelf edge to the south (both encompassed by our models), there are no significant topographic features along or near the profile that could otherwise distort the MT responses. Station positions were determined by the ship's GPS position at the drop location. A total of 14 WHOI and 10 SIO MT stations were deployed.

SIO instruments were deployed as part of a combined MT and controlled source EM survey to map shallow offshore groundwater, and so some SIO sites were collocated with previous WHOI deployments. WHOI instruments were deployed for 3 months, whereas SIO instruments were on the seafloor for only 3 days. Of the instruments deployed, we use data from 15 stations (9 WHOI and 6 SIO stations). Three WHOI instruments were lost: one was dredged up by fishing activity and returned to us, one was released from its anchor (also possibly due to fishing activity) and recovered in the Canary Islands after it drifted across the Atlantic, and the third was a deep water site deployed off of this profile.

The magnetotelluric time series data from WHOI stations were manually checked; noise and obvious outliers were removed from the data set. The data were then rotated to magnetic north and referenced to two remote stations. The first reference station was installed on Martha's Vineyard (~30 km NNW to the MT array) for the duration of the marine deployments, and the second was selected from the remaining marine stations. The data were processed using the Bounded Influence Remote Reference Processing (BIRRP) algorithm [Chave and Thomson, 2003, 2004]. Data from the SIO instruments were processed using the multiple station array processing routine of Egbert [1997].

The broadband sensors on SIO instruments provided consistent responses with minimal noise at periods between 0.1 and 1000 s and the long period sensors on the WHOI instrument exhibit responses of equal criteria at periods of 10–10,000 s (Figure 2). Since the stations were located in shallow water depths, passing tidal waves introduced motional noise to the data. Both the SIO and WHOI instruments exhibit this wave noise in the 1–10 s band. Outside of this noise band, the responses are high-quality, with very high-quality 1-D responses at 0.1–1 s periods on the SIO instruments. No complex processing schemes were required for the short period data, and responses from collocated SIO and WHOI instruments show similar trends within a period band between 10 s and 1000 s (w6 and s8, w4 and s10), as presented in Figure 2.

For an ideal 2-D Earth, the magnetotelluric transverse electric (TE) mode corresponds to electric currents flowing parallel to the geographical electrical strike, whereas the transverse magnetic (TM) mode corresponds to current flowing perpendicular to strike. To seek the regional geoelectric strike, we examined the magnetotelluric polar diagrams [Berdichevsky and Dmitriev, 2008] and phase tensors [Caldwell *et al.*, 2004; Booker, 2014], as shown in Figure 3. This analysis indicates a geoelectric strike azimuth of 75°, as derived from the median value of the polarization ellipses for periods longer than 100 s where the data are 2-D. Thus, the geoelectric strike is roughly perpendicular to the MT profile and approximately 30° to the regional rift and fault features. Station w4 shows a strike angle that is ~5–7° larger than s10 (Figure 3b). This discrepancy may arise from small errors in the accuracy of the compass sensors installed on these particular instruments. The strike direction of stations w6 and s8 perfectly match. At periods shorter than 1 s, the TM and TE mode data are equal to within the estimated uncertainty (Figure 2). Therefore, the high-frequency responses are purely 1-D with no signs of a static shift, which is expected for the uniform conductivity of the shallow sedimented seafloor.

The phase tensors show two distinct patterns that are segmented to the north and south of site s3. The phase tensors and polar diagrams for the south group (w9–w3) are consistent with each other, showing equivalent data dimensionality and strike angles (Figure 3b). The phase tensors and polar diagrams for the north group (w14–w11) exhibit moderately inconsistent strike angles. This coincides with a substantial change in the TE phase behavior between the two groups of stations (Figure 2), which could be related to a

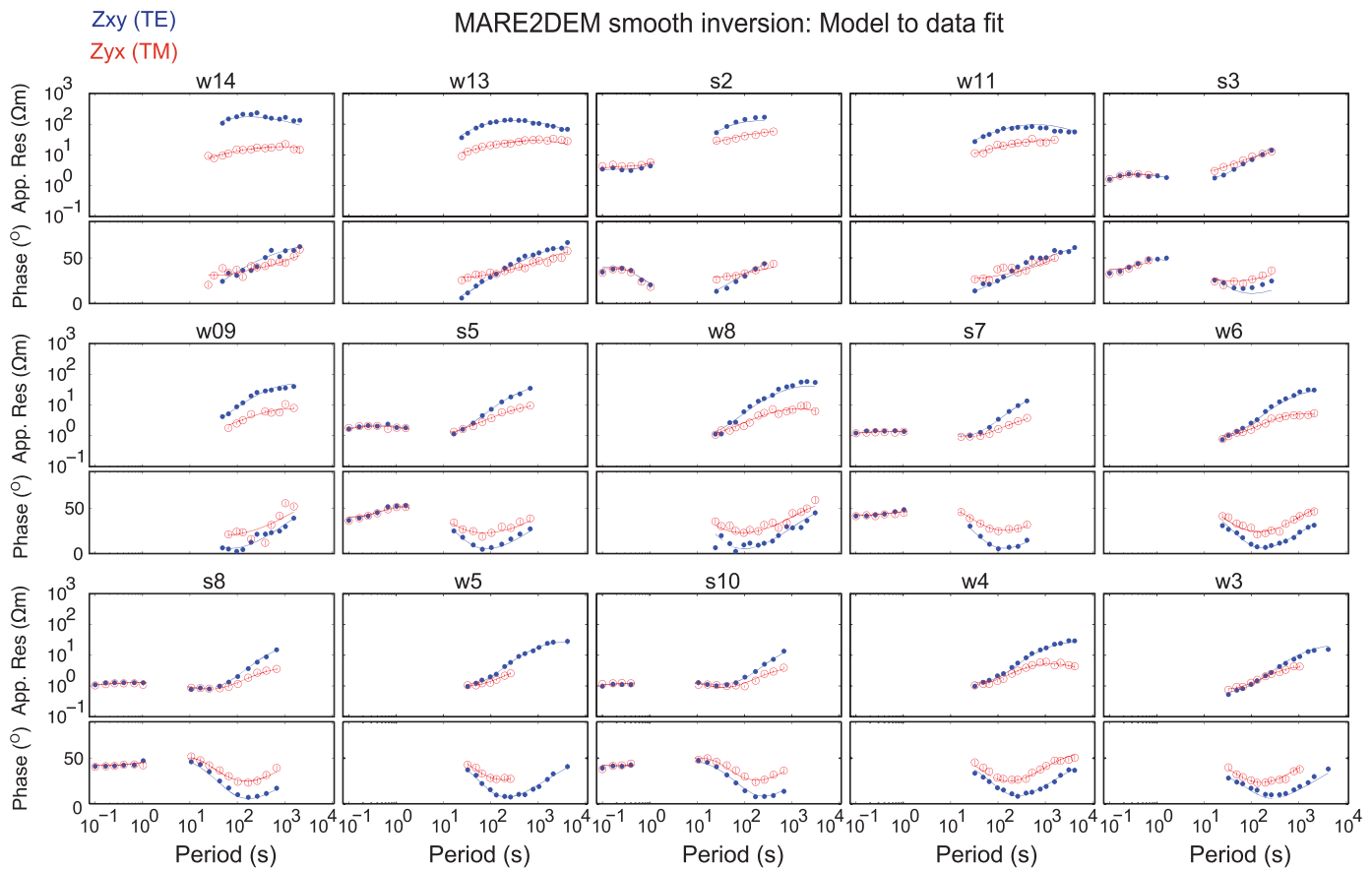


**Figure 2.** The model fit to the TE (blue) and TM (red) modes apparent resistivity and phase data, for 15 MT stations. WHOI MT stations: w3, w4, w5, w6, w8, w9, w11, w13, and w14. SIO MT stations: s2, s3, s5, s7, s8, and s10. The lines represent the model, and the dots represent the data. The azimuths of the TE and TM modes are 75° and 165°, respectively.

lateral change in the resistivity structure, presumably indicative of anisotropy (further discussion in section 4). The phase tensor skew angles ( $\beta$ ) in the north group are mostly consistent with two-dimensional data but sporadically exceed 5° at periods shorter than 60 s and longer than 1000 s. For station s3, the  $\beta$  values exceed 5° and the polar diagrams are uniquely anomalous and distorted at all periods, indicative of regional 3-D induction effects [Jones, 2012]. Nevertheless, excluding data from s3 in the inversions resulted in a model that differs insignificantly from our smooth models. Hence, we assume that the higher dimensionality of s3 does not affect our preferred conductivity model.

### 3.2. Inversion Schemes

In this study, we applied two different inversion schemes to jointly invert the apparent resistivity and phase data of both TE (Zxy) and TM (Zyx) modes. First, we inverted the data using a 2-D nonlinear conjugate gradients method [Rodi and Mackie, 2001]—a regularized inversion that is implemented in the WinGLink software package (Geosystem srl). Second, the data were inverted using MARE2DEM, a 2-D nonlinear regularized inversion method that employs a parallel goal-oriented adaptive finite element algorithm [Key and Ovall, 2011; Key, 2016], which is conceptually based on the Occam inversion approach [Constable et al., 1987; deGroot Hedin and Constable, 1990].

We ran a series of inversion tests with various starting models, error floors, and regularization parameters, which were applied independently to both WinGLink and MARE2DEM, to seek the ideal conductivity model in terms of root-mean-square (RMS) misfit value, smoothness, and geological plausibility. Compared with WinGLink's structured scheme, MARE2DEM utilizes unstructured adaptive finite elements for the forward solver, enabling us to accurately incorporate sharp topographic features in the mesh. Furthermore, MARE2DEM allows construction of a much higher resolution mesh while still converging at lower computational

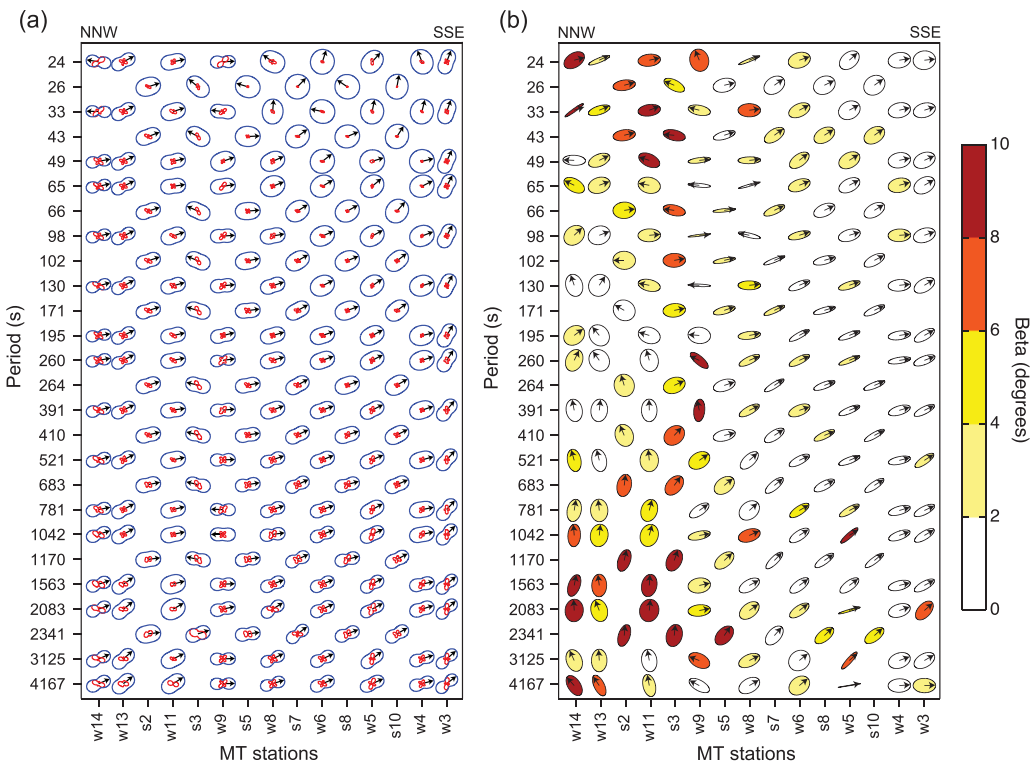


**Figure 3.** Polar diagrams and phase tensor ellipses for all MT stations. (a) Polar diagrams of the magnetotelluric transfer function. The blue and red lines show the rotated off-diagonal and diagonal components of the transfer functions, respectively. The arrows show the rotation angle that maximizes the off-diagonal component, which is indicative of the geoelectric strike. The short-period data are predominantly 1-D, and transition to 2-D at longer periods. (b) Phase tensor ellipses of the magnetotelluric transfer function. The fill color represents the beta angle, which provides a measure of the data dimensionality. The majority of the data are 1-D or 2-D, with beta angles of less than 4°. The arrows point in the direction of the geoelectric strike angle.

cost than the sparser WinGLink mesh. Therefore, the WinGLink inversion scheme was only used for the initial smooth inversion whereas MARE2DEM was applied for the rest of the models. The purpose for using both the WinGLink and MARE2DEM inversion algorithms is to increase the level of confidence in the initial smooth models, before the construction and run of various a priori models that are essential to yield an ideal preferred model.

All of the models presented here are 290 km in length and 250 km deep, whereas the MT stations are located horizontally between 65 km (NNW) and 200 km (SSE) along the model space (Figure 4). The coastline is located less than 50 km NNW of the MT profile, and the continental shelf edge is ~30 km SSE from the MT array (Figure 1a). Both the coastline and the bathymetric slope at the shelf edge are included in our models.

### 3.2.1. WinGLink Inversion Properties

WinGLink enables the automatic generation of a finite-difference model mesh. We modified the automated mesh to create a grid of 70 rows by 274 columns. The mesh grid was finely discretized around each MT station and gradually coarsened with depth and distance from the profile edges (Figure 4a). This particular mesh was chosen based on computational cost and model reliability. The penalties for horizontal and vertical variations in the model resistivity were kept at the default setting of 1.5 and 1.8, respectively. The smooth inversions were started from a  $10\ \Omega\text{m}$  half-space model, and additional a priori models with different hypothetical structures were tested. The data error floors were set to 10% for the apparent resistivity and 5% for the phase. We varied the smoothness regularization parameter ( $\tau$ ) value between 0.01 and 3 to obtain the optimal fitting model while avoiding overfitting to maintain a realistic conductivity structure. Higher  $\tau$  values generally produce smoother models with poorer fits to the data, whereas low  $\tau$  values lead to rough models with good fits to the data. For an RMS misfit target of 1.5, a  $\tau$  value of 0.1 led to a smooth model with good fits to the data.

### 3.2.2. MARE2DEM Inversion Properties

The MARE2DEM models were parameterized using unstructured fine quadrilateral mesh elements that gradually increase in size as a function of depth, which were bounded by an unstructured coarse triangular

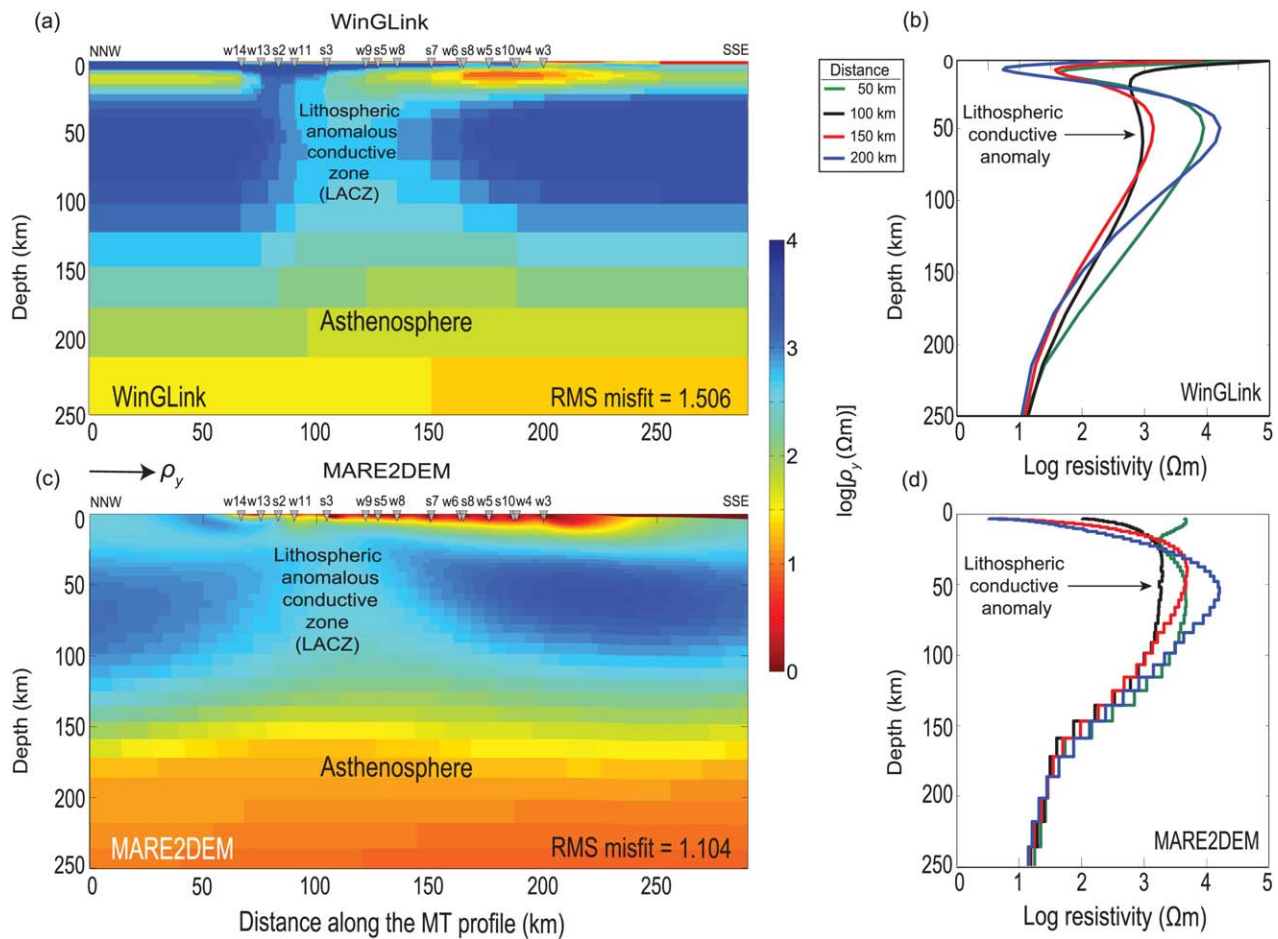


**Figure 4.** 2-D isotropic smooth inversion models presented in a  $\log[\rho_y (\Omega m)]$  color scale: (a) WinGLink 2-D MT conductivity model. (b) Depth-resistivity profiles, extracted from the WinGLink 2-D model horizontally at 50, 100, 150, and 200 km. (c) MARE2DEM MT conductivity Model. (d) Depth-resistivity profiles, extracted from the MARE2DEM model horizontally at 50, 100, 150, and 200 km. The inverted triangles denote the WHOI (w) and SIO (s) magnetotelluric station locations.

grid, resulting in  $\sim 10k$  free parameters (Figure 4c). Spatial variations in the model resistivity were penalized with 3:1 horizontal to vertical ratio. The apparent resistivity of the TE and TM modes were inverted in their  $\log_{10}$  forms, thus increasing the inversion robustness and reducing the convergence time [Wheelock *et al.*, 2015]. The data error floors were assigned to be 10% for both the apparent resistivity and phase.

We performed isotropic and triaxial anisotropic inversions, which employed 10  $\Omega m$  half-space as starting models. The triaxial anisotropic inversion solves for resistivity in three directions; perpendicular to the MT array ( $\rho_x$ ), parallel to the MT array ( $\rho_y$ ), and in the vertical direction ( $\rho_z$ ). This inversion method allows the user to penalize anisotropy and thus limit the amount of anisotropy in the inverted model [Key and Ovall, 2011; Naif *et al.*, 2013]. To determine if anisotropy is required by the data, we inverted the data with anisotropy penalties ranging from 0.1 to 1, where a penalty of 1 produces isotropic models. For the smooth anisotropic inversion that was minimally penalized (anisotropy penalty of 0.1), the ratio between the two horizontal models ( $\rho_y/\rho_x$ ) shows insignificant anisotropy. However, the  $\rho_y/\rho_x$  ratio of the anisotropic inversion using our preferred model, suggests the presence of a moderate anisotropy through the LACZ and immediately beneath it (further information in section 4.4.1).

The TE and TM mode data were jointly inverted to different RMS misfit targets that ranged from 1.0 to 1.5. An RMS misfit target of 1.1 was found to be ideal, using combined criteria of model smoothness, overfitting avoidance, and model to data fit.

### 3.2.3. Model to Data Fits

The WinGLink smooth inversion converged to an RMS misfit target of 1.5 after 22 iterations while the MARE2DEM smooth inversion converged to an RMS misfit target of 1.1 after 16 iterations. The TE and TM mode

data and MARE2DEM inversion model responses for the MT stations are shown in Figure 2. All stations present adequate model fits for both the apparent resistivity and phase data. The TE and TM mode short period data (0.1–1 s) from SIO instruments are equivalent (Figure 2), which is indicative of a 1-D conductivity structure as is expected for the uppermost sedimentary units seen in the region [Siegel *et al.*, 2014].

## 4. Results

To describe the conductivity structure beneath the eastern North American passive margin, we present two-dimensional isotropic smooth inversions, constructed using two different inversion methods as described above. By utilizing the inversion Jacobian sensitivity matrix, the model spatial sensitivity to resistive and conductive structures was determined. The depth of the LAB was constrained using various test models. Inversions in which a discontinuity was introduced as well as runs including a priori information were implemented, along with forward modeling tests to validate models returned.

### 4.1. 2-D Isotropic Smooth Inversion Models

Despite the different model parameterizations, algorithms, and final misfits, both inversion schemes returned similar conductivity structures.

A large shallow conductor is observed along both models between ~160 and 225 km horizontally at ~7–10 km depth (Figures 4a and 4c). In the WinGLink inversion, this shallow conductor is capped by a strong resistor whereas in the MARE2DEM inversion it extends to the surface. This strong conductor consistently appears in all of the initial inversion models produced by WinGLink and MARE2DEM, located in a region where the data are highly sensitive to the inversion model parameters (further information in section 4.2). Thus, we are confident that this shallow conductor is a real feature and not an inversion artifact, possibly resulting from high porosities in the thick sediments and upper crust [Siegel *et al.*, 2014]. Resistive structures of ~1–3 k  $\Omega$ m are observed horizontally between 0–75 and 150–290 km along the profile, extending vertically between ~25 and 110 km depths (Figures 4a and 4c). High resistivity at this depth range is representative of the oceanic lithosphere [Cox *et al.*, 1986].

Between the resistive structures at the model flanks, a ~350  $\Omega$ m lithospheric anomalous conductivity zone (LACZ) appears, positioned at ~75–150 km horizontally along the profile (Figures 4a and 4c). Figures 4b and 4d present resistivity-depth profiles at different horizontal distances across the model space. These profiles emphasize the contrast between the resistive lithospheric regions and the LACZ, down to a depth of about 150 km. Below ~200 km depth, the vertical profiles show a resistivity of 10–30  $\Omega$ m (Figures 4b and 4d) that is typical for asthenosphere [Sarafian *et al.*, 2015]. Both the WinGLink and MARE2DEM smooth inversion models show a lithosphere that thins from the NNW continental crust to the center of the profile, followed by a lithospheric thickening from the model center toward the SSE oceanic crust.

At depths between ~100 and 200 km the model resistivity decreases moderately from approximately 2.5 k  $\Omega$ m (lithospheric upper mantle) to ~15  $\Omega$ m (asthenosphere), as shown in Figures 4a and 4c. This gradual transition between the resistive lithosphere and conductive asthenosphere is attributed to the inversion smoothing process, and thus, yielding an elusive LAB. Inversion smoothing effects can often be mitigated by applying model tests where the regularization scheme is modified (see section 4.3). In this study, we aim to resolve the depth and topography of the LAB.

### 4.2. Sensitivity Analysis

The sensitivity of the MARE2DEM Occam based inversion is effectively computed from the model Jacobian matrix ( $J$ ) [Constable *et al.*, 1987; MacGregor *et al.*, 2001; Key, 2016]. The Jacobian sensitivity matrix evaluates the data sensitivity to model parameters. We performed a linearized sensitivity analysis, carried out in the manner of Schwanenberg *et al.* [2002] where the rows of the uncertainty weighted Jacobian matrix are summed over all data and normalized by the area of each parameter cell. Since the linearized sensitivity is a relative measure, we plot them as percentiles, where, for example, a value of 0.3 implies that the sensitivity is at the 30th percentile level. Figure 5 shows the MARE2DEM smooth inversion, superimposed by the  $J$  contours that illustrate the spatial sensitivity to variations in resistivity (e.g., 0.7 contour = 70% sensitivity). A contour value  $\geq 0.15$  demonstrates a level of sensitivity that is sufficient to resolve the corresponding resistivity structure. Values above 0.5 are considered to represent a high level of sensitivity. The highest sensitivity appears at the shallow region (75–80% sensitivity) beneath the MT stations and declines moderately to a

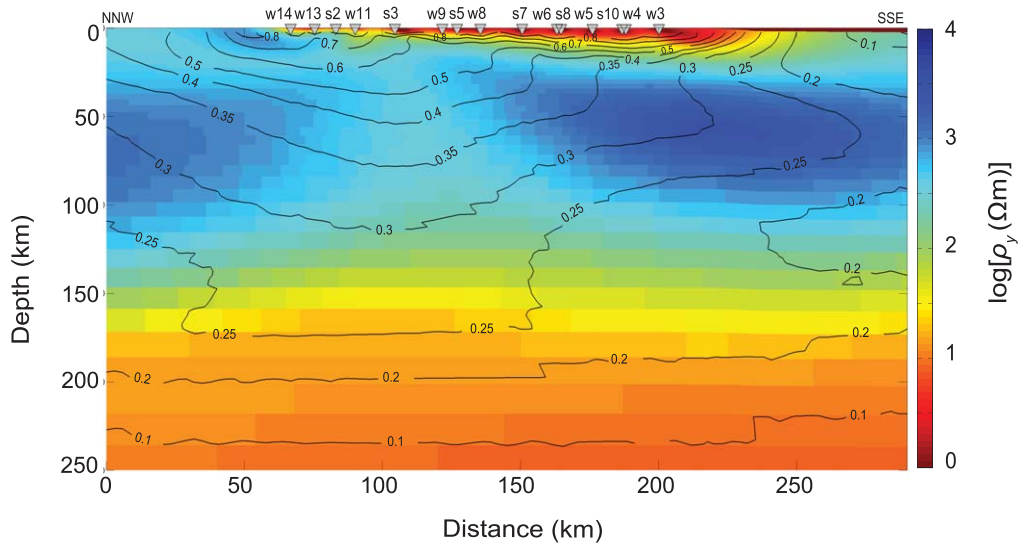


**Figure 5.** MARE2DEM smooth inversion model in a  $\log_{10}$  scale, superimposed with the Jacobian sensitivity contours that illustrate the inversion sensitivity to spatial variations in resistivity. The contours value indicates the level of the data sensitivity to the model parameters (e.g., 0.2 = 20% sensitivity). The inverted triangles represent the MT stations positions.

minimum 10% sensitivity at  $\sim 235$  km. The model exhibits satisfying sensitivity down to a depth of  $\sim 150$  km, both at the NNW model edge  $\sim 65$  km before the first MT station (w14) and from SSE,  $\sim 90$  km after the last station (w3).

As is typical for MT data, the model shows higher sensitivity to conductive regions, where current flow is concentrated. Consequently, the sensitivity spreads across the model in a parabolic fashion (approximate U-shape), exhibiting downward extending high sensitivity at the LACZ area ( $\sim 72$ – $125$  km horizontally,  $\sim 175$  km vertically) that gradually decreases toward the edges (Figure 5). Deeper than  $\sim 175$  km, the sensitivity is equally distributed laterally and only varies with depth. The data are insensitive to any structure below  $\sim 240$  km depth (Figure 5). Thus, we restrict our interpretation to depths shallower than  $\sim 225$  km, where the data sensitivity is greater than 15%.

#### 4.3. Model Tests

The smooth inversion models (Figure 4) provide a satisfying initial imaging of the subsurface; yet, further modeling is required to determine the underlying conductivity structure, with a higher level of accuracy. For this purpose, we generated a series of test models which were particularly designed to: (1) verify the existence of the LACZ; and (2) constrain the depth and topography of the LAB. To achieve these aims, we modified the inversion regularization and examined the forward and inverse responses of different a priori starting models.

##### 4.3.1. LACZ Tests

The LACZ is a persistent feature that appears in all of our converged smooth inversion models. Nevertheless, we performed two different model tests to confirm the authenticity of the LACZ. First, we superimposed a  $1\text{k }\Omega\text{m}$  resistor on top of the smooth model LACZ and ran a forward calculation (Figure 6a). In such a test, the aim is to examine whether the added resistor reduces the model to data fit, and thus, provide evidence to the validity of the tested feature. We performed a normalized residuals comparative analysis between the smooth model and the forward model test which indicates that the model to data fits of the apparent resistivity and phase were reduced both for the TE and TM modes (Table 1). Hence, the residuals analysis supports the notion that the LACZ is most probably an essential feature and not an artifact.

Second, a  $3\text{k }\Omega\text{m}$  horizontal layer was positioned between 25 and 100 km depth, forced upon the LACZ and the resistive lithosphere of the smooth model (penalty weight = 1.0). In this type of prejudiced model test, the inversion is penalized for any deviation from the a priori starting model. Therefore, if such model alteration occurs, it confirms the robustness of the examined feature (e.g., LACZ). Here the prejudiced model test converged to an RMS misfit of 1.098 while deviating significantly from the a priori model by reducing

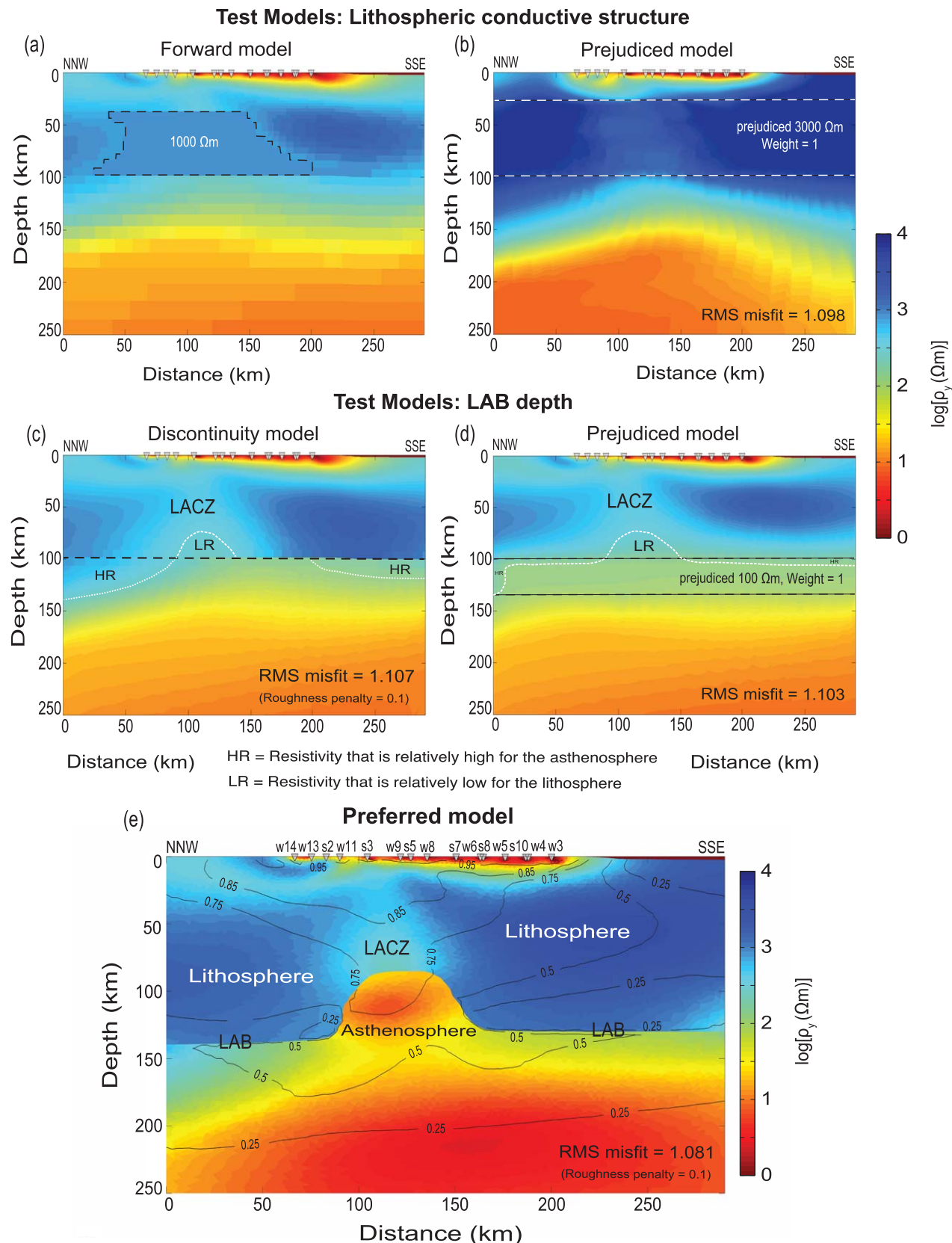


Figure 6.

**Table 1.** A Table Comparison Between the Normalized Residuals RMS of the Forward Model Test and the Smooth Model, for Both the TE and TM Modes<sup>a</sup>

Data Type	Smooth Model RMS	Test Model RMS	Models RMS Difference (%)
TE apparent resistivity	0.87	0.91	4.4%
TE phase	0.72	0.74	2.7%
TM apparent resistivity	0.71	1.09	34.8%
TM phase	0.81	1.02	20.6%

<sup>a</sup>The forward test model increased the residuals of the TM mode significantly more than the TE mode residuals. The percentage RMS difference between the two models represents the reduction in the model to the fits, as imposed by the forward model test. The models RMS values were calculated from the normalized residuals of all MT stations, at all frequencies.

w9, alternatively and jointly. Stations s3 and w9 are located directly above the LACZ, and present moderate to high phase tensor  $\beta$  values (Figure 3b). In these three inversion tests the LACZ remained, and the overall conductivity model did not alter significantly. These three tests strongly suggest that the LACZ is a robust geological feature that is required by the data.

#### 4.3.2. LAB Tests

To better constrain the depth variations of the LAB, we performed (a) an inversion with an imposed discontinuity, (b) a prejudiced inversion, and (c) forward models based on the final smooth model. Seismic phase conversions of S-to-P ( $S_p$ ) and P-to-S ( $P_s$ ) analysis for data sets acquired beneath eastern North America, suggest the presence of a sharp seismic velocity discontinuity located at  $\sim 85$ –111 km depth, which is attributed to the LAB [Rychert et al., 2005, 2007; Abt et al., 2010; Rondenay et al., 2017].

To resolve the ambiguity observed in our smooth models (Figure 4) concerning the depth variations of the LAB, we forced upon the starting model a horizontal discontinuity at a depth of 100 km (Figure 6c) that is roughly at the LAB discontinuity depth, as inferred from seismic phase conversion studies [Rychert et al., 2007; Rondenay et al., 2017]. In this type of inversion, the roughness penalty is decreased across the imposed discontinuity, thus enabling the inversion to include sharp transitions in resistivity along the discontinuity boundary if such are favored by the data. The discontinuity inversion converged to an RMS misfit of 1.107, presenting a relatively high resistivity (HR) for the upper mantle below the 100 km imposed discontinuity at the NNW edge of the model (Figure 6c). This HR region suggests that the LAB in the NNW has a relatively moderate resistivity gradient across it and is deeper ( $\sim 140$  km), extending  $\sim 90$  km horizontally along the profile. Toward the SSE end of the model, a much sharper LAB is observed, extending to a depth of  $\sim 130$  km as indicated by the HR region. Thus, the adjustment applied to the regularization was proven to be efficient in resolving sharp transitions in resistivity where it is required by the data (Figure 6c). Above the 100 km forced discontinuity, a relatively low resistivity (LR) region of  $\sim 100 \Omega\text{m}$  exists, untypical for oceanic lithosphere. This LR region curves upward to a depth of  $\sim 85$  km into the LACZ between  $\sim 90$  and 145 km laterally (Figure 6c). The forced discontinuity did not significantly alter the model fit to the data, and so the evidence is equivocal as to whether a relatively sharp LAB is present.

Next, we conducted a prejudiced model test to determine how robust are the asthenospheric HR regions that emerged from the discontinuity model test. These HR regions located at the model edges varied significantly from the  $100 \Omega\text{m}$  at the model center (beneath the discontinuity). Based on the  $100 \Omega\text{m}$  asthenospheric resistivity, we inverted the data with an a priori starting model that includes a  $100 \Omega\text{m}$  weighted layer (penalty weight = 1.0). The  $100 \Omega\text{m}$  forced layer extends laterally throughout the entire model and vertically between 100 and 140 km (Figure 6d). In this inversion, the HR regions slightly altered the prejudiced a priori model, mainly in the immediate area beneath 100 km depth (Figure 6d). This confirms the existence of moderate HR regions, and consequently, supports the depth variability of the LAB across the model.

**Figure 6.** Test and preferred models: (a) Forward model with  $1 \text{k } \Omega\text{m}$  superimposing the LACZ (dashed contour) observed in the MARD2EM smooth model (Figure 2c, RMS misfit = 1.104). (b) Model with lithospheric resistivity prejudiced to  $10 \text{k } \Omega\text{m}$  between 25 and 100 km depth. (c) Model with forced discontinuity (roughness penalty of 0.1) at 100 km depth. The horizontal discontinuity is marked by a black dashed line. Relatively high and low resistivity (HR and LR) areas are bounded between the black and white dashed lines. (d) Model with a  $100 \Omega\text{m}$  prejudiced layer between 100 and 140 km depth (black dashed lines), indicated by the black dashed lines. LR and HR areas are denoted by the white dashed line. (e) The preferred 2-D isotropic conductivity model in  $\log[\rho/\Omega\text{m}]$  color scale. The contours value indicate the level of the data sensitivity to the model parameters (e.g.,  $0.25$ – $0.5$  = 25–50% sensitivity across the LAB).

the  $3 \text{k } \Omega\text{m}$  forced resistor to  $\sim 800 \Omega\text{m}$ , at the LACZ location (Figure 6b). Thus, despite the applied penalization the LACZ still emerged from the data, providing sufficient evidence for its authenticity.

It is also possible that the LACZ is the manifestation of high dimensionality data. To test a scenario in which the LACZ is a result of 3-D conductive effects, we ran smooth inversion tests without the data from stations s3 and

#### 4.4. Preferred Model

The information derived from the various test models was utilized to optimize the initial smooth, isotropic model, and thus, yield a well-constrained final model. This constraint was done by inverting the data with a horizontally varying forced discontinuity (roughness penalty = 0.1, consistent with the model shown in Figure 6c), which tracks the LAB LR and HR regions detected in the test models (Figures 6c and 6d). Figure 6e shows our discontinuity driven preferred model, where the depth of the LAB varies from ~145 km at NNW to ~85 km beneath the LACZ to ~130 km at SSE of the model. Across the LAB, over less than ~8 km depth range three distinctive declines in resistivity are observed; (1) ~800 to ~250  $\Omega\text{m}$  in the NNW, (2) ~350 to ~30  $\Omega\text{m}$  in the center (asthenospheric rise area), and (3) ~1000 to ~90  $\Omega\text{m}$  at the SSE edge of the model. Apart from the LACZ, the lithosphere is more pronounced and vertically extended (particularly in the SSE) than observed in the smooth model, since the applied discontinuity significantly reduces the inversion smoothing (Figure 4c versus Figure 6e). The LACZ in this model is well associated with the central asthenospheric rise.

The Jacobian sensitivity matrix of the isotropic preferred model was calculated and is shown in Figure 6e. The  $\mathbf{J}$  sensitivity matrix indicates that discontinuity applied to this model significantly improved the data sensitivity to the model parameters throughout the entire model when compared to the smooth model  $\mathbf{J}$  sensitivity (Figure 5). The NNW part of the model shows a higher sensitivity than the SSE edge. Highest  $\mathbf{J}$  sensitivities are present at the top of the model (90%) and the LACZ (85%). The rising asthenosphere beneath the LACZ enhances the depth extension of the data sensitivity considerably, as evidenced by the 0.75 parabolic contour. Across the LAB the  $\mathbf{J}$  sensitivity increases from 25% to 50%, and thus suggests that the apparent contrast in resistivity is favored by the data. An RMS model to data fit comparison between the smooth and preferred model, demonstrate that the preferred model improved the RMS misfits by approximately 5%, for both the apparent resistivity and phase of the TE and TM modes.

##### 4.4.1. Anisotropy

Anisotropic inversion applied to the MARE2EM smooth model with minimal penalization for anisotropy (0.1), resulted in a model with insignificant anisotropy. Since the isotropic preferred model improved both the data sensitivity to the model parameters and the RMS misfit, we ran an anisotropic inversion to the preferred model. The penalty for anisotropy was set to 0.1 and the RMS misfit target to 1.1 (consistent with the smooth anisotropic inversion). The  $\rho_y/\rho_x$  anisotropy ratio of this anisotropic inversion indicates that anisotropy varies both laterally and vertically along the profile (Figure 7). The anisotropy is most prominent in the region surrounding the LACZ and the asthenospheric rise. At the LACZ, the resistivity parallel to the geoelectric strike, represented by  $\rho_x$  is 1.4 times greater than the resistivity along the MT profile. The moderate anisotropy diminishes and becomes nearly isotropic to the SSE of the LACZ. The evolving lithospheric anisotropy also correlates with distinct behavior patterns seen in the data and phase tensors, where the

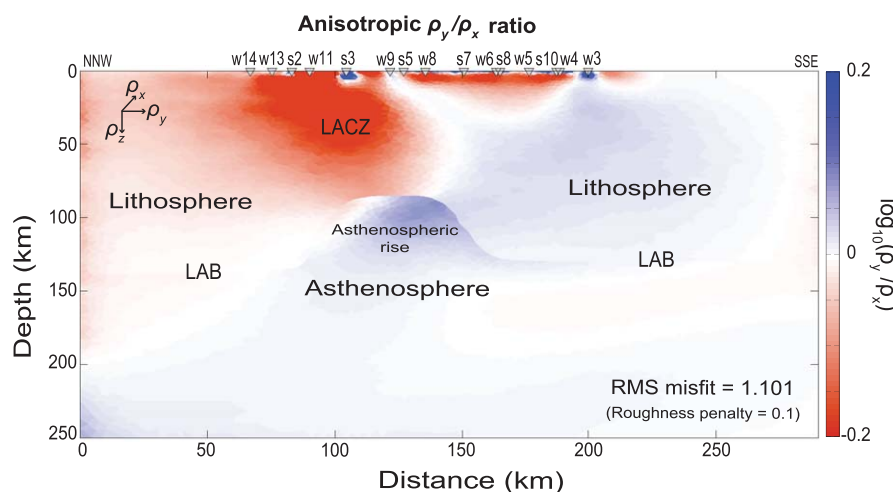


**Figure 7.** The  $\rho_y/\rho_x$  ratio of the anisotropic inversion applied to the preferred model. The color scale shows  $\log_{10}(\rho_y/\rho_x)$ . Distinctive anisotropy exist at the LACZ (intense red) perpendicular to the MT profile, as represented by  $\rho_x$ . At the asthenospheric rise,  $\rho_y$  is about 1.3 times greater than  $\rho_x$ .

anisotropic LACZ and the relatively isotropic regions are coincident with the NNW and SSE group of sites, respectively, as discussed in section 3.1. At the asthenospheric rise, the  $\rho_y/\rho_x$  ratio is switched ( $\sim 120$ – $160$  km along profile), exhibiting higher resistivity parallel to the MT profile ( $\rho_y$ ) than along the geoelectric strike ( $\rho_x$ ).

By incorporating the information obtained from the test models and applying isotropic/anisotropic inversions, we were able to: (1) validate the necessity of the LACZ to fit the data; and (2) mitigate the inversion smoothing effect by applying discontinuity, as derived from seismic constraint. Consequently, we produced the best possible final model that adequately describes the spatial transitions in resistivity and the variability in LAB topography.

## 5. Discussion

The various MT inversion models presented here suggest that the depth of the LAB beneath the study region varies between  $\sim 85$  km (model center) and  $\sim 130$ – $145$  km (model flanks). A vertical LACZ exists throughout the lithosphere at the center of all the inversion models. The anisotropic inversion applied to the preferred model suggests that only a moderate amount of anisotropy exists at this rifting margin. To assess and interpret these results in a broader sense, we examined the regional shear-wave velocity model,  $P_S$  receiver function, and gravity data. The purpose of this comparison is to identify similar large-scale trends between the models rather than localized features, which is infeasible due to resolution incompatibilities.

### 5.1. Shear-Wave Velocity and $P_S$ Receiver Function

Shear-wave velocity ( $V_S$ ) and resistivity are both sensitive to physical properties such as temperature, melt, water content, and lithology [e.g., Jones *et al.*, 2013]. Different rock composition will affect the sensitivity and resolution of each method, with seismic velocity much more sensitive to chemical composition. However, a comparison between  $V_S$  and resistivity models may contribute to a more comprehensive understanding of the underlying regional structure. Our study area is located nearshore, away from land-based seismic stations across the eastern North America, limiting the coverage of regional and local seismic studies [e.g., Schaeffer and Lebedev, 2014]. However, the LAB can still be identified from the decrease in  $V_S$  imaged by global models [e.g., S40RTS, Ritsema *et al.*, 2011; SAVANI, Auer *et al.*, 2014; SL2013NA, Schaeffer and Lebedev, 2013; SEMum2 and SEMUCB-WM1, French *et al.*, 2013; French and Romanowicz, 2014].

Here we chose to employ the SEMum2 global  $V_S$  model by French *et al.* [2013]. This model includes 99,000 waveform windows (over 5 million data points), comprising a single data set that enables a harmonized parameterization. Figures 8a and 8b shows  $dV_S$  horizontal and vertical slices derived from the SEMum2 global model. These cross sections show variations in velocity that are presented on a regional scale, corresponding to our region of study. We emphasize that a global  $V_S$  model offers limited resolution on a regional/local scale, and therefore, unlikely to resolve the asthenospheric rise and LACZ given their isolated extent. Thus, the  $V_S$  model is used here solely to identify general trends for comparison with the resistivity preferred model.

The regional scale  $V_S$  horizontal slice at 100 km depth shows a trend of high-low-high  $V_S$  (Figure 8a) in the vicinity of the MT stations. This  $V_S$  trend is viewed better in the vertical slice, across the lithosphere from NNW to SSE (Figure 8b), roughly coinciding with the high-low-high lithospheric resistivity trend (as observed in our preferred model, Figure 6e). These two-independent studies add support to a possible alteration in lithology at this region. A decrease in  $dV_S$  observed in the vertical slice at depths of approximately 100–125 km indicates the depth range of the LAB. Such decrease in  $dV_S$  is also noted in other recent global models [e.g., SEMUCB-WM1, French and Romanowicz, 2014; SAVANI, Auer *et al.*, 2014; S40RTS, Ritsema *et al.*, 2011], suggesting that the depth range of the LAB in this region is  $\sim 75$ – $130$  km.

An analysis of  $P$ -to- $S$  receiver function (RF) data [Rondenay *et al.*, 2017] from a seismic station located  $\sim 35$  km from the nearest MT station (Figure 1a) exhibits a strong negative  $P_S$  phase at 109 km depth. This phase is indicative of the LAB, and is comparable to nearby LAB depths determined by Rychert *et al.* [2005, 2007] (87–105 km) and Abt *et al.* [2010] ( $111 \pm 7$  km).

Since the LAB depth from our preferred conductivity model ranges between  $\sim 85$  and  $145$  km (average of  $115$  km), it agrees well with previous seismic tomography, receiver functions, and conductivity studies, and thus, add confidence to our results.

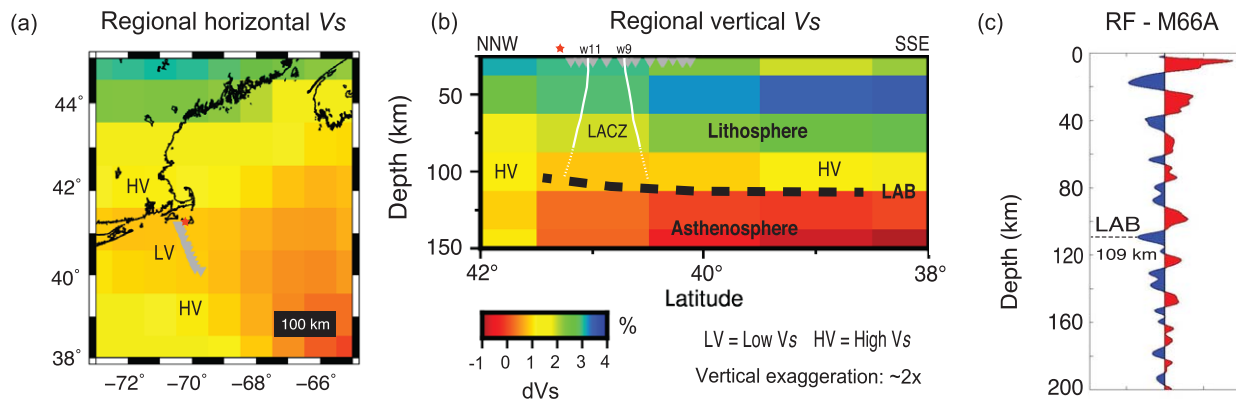


**Figure 8.** Regional shear velocity variation across the study area, from a  $1^\circ \times 1^\circ$  resolution global SEMum2  $V_s$  model [French *et al.*, 2013]. (a) Map showing the lateral  $V_s$  variation at 100 km depth. Black contour represents the coastline; gray triangles denote the MT stations, and red star denotes the location of the RF-M66A teleseismic station. (b) Vertical cross section at  $-70^\circ$  longitude showing the decrease in velocity across the LAB. Red and blue shades indicate slower and faster  $V_s$  velocity, respectively, from the model reference. The dashed black line indicates the LAB, which shallows to the NNW to match the LAB depth detected by the RF-M66A station that is located vertically above that zone, marked by a red star. The gray triangles denote the MT stations. White lines show the LACZ region, as derived from the preferred MT model. (c)  $P_s$  RF profile, as produced from the data recorded by the M66A teleseismic receiver, situated in the Nantucket Island,  $\sim 35$  km from w14 MT station (Figure 1a). The RF data is taken from the GLImER database [Rondenay *et al.*, 2017].

### 5.2. Regional Gravity Anomaly

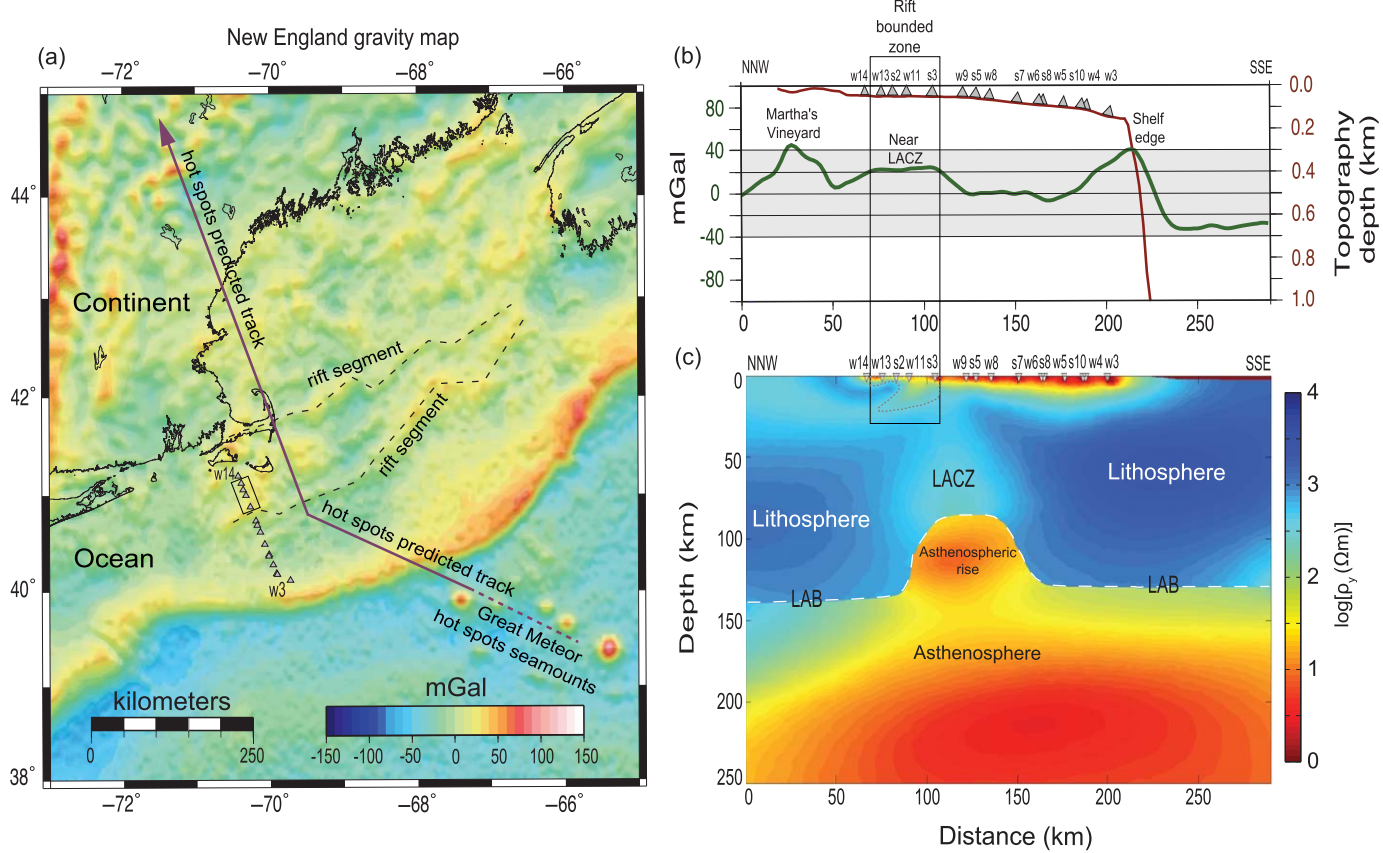
Marine gravity anomalies are vital for constraining global tectonics and continental margin structures and assist in characterizing rifting and sedimentation processes [e.g., Laxon and McAdoo, 1994; McAdoo and Laxon, 1997; Cande *et al.*, 2000; Wyer and Watts, 2006; Bassett and Watts, 2015]. Here the New England continental margin gravity data were extracted from a global gravity model, based on  $1 \times 1$  min satellite-derived free-air gravity anomaly grid [Sandwell *et al.*, 2014].

Figure 9a presents a regional gravity map across the New England continent-ocean boundary, superimposed by the MT profile. We note that the MT array is spread over a relatively flat seafloor bathymetry (Figure 9b). Nevertheless, three gravity anomalies are detected along the model profile, as shown in Figure 9b. The positive gravity anomalies in the NNW and SSE are associated with Martha's Vineyard and the continental shelf edge. In addition to these two distinctive anomalies, we identified a moderate positive gravity anomaly ( $\sim 20$  mGal) that is located between two subparallel crustal rift segments that exhibit anomalies of  $\sim 15$ – $30$  mGal. The  $\sim 20$  mGal anomaly is partially overlapping the LACZ from NNW, collocated with a vertically extended seafloor conductor that becomes significantly thicker beginning at 100 km distance along the profile, and thus, represents a thickening sediment package (Figures 9b and 9c). A seismic reflection line that coincides with our MT profile presents a thicker wedge of Pleistocene sediment beneath the profile center [Siegel *et al.*, 2014]. Further, the LACZ and thinning lithosphere occur between  $\sim 100$  and 150 km. Both of these observations together represent lower densities and likely cause the large reduction seen in the gravity anomalies between  $\sim 100$  and 120 km along the profile. Then, a combination of thinning sediments, more resistive lithosphere, and deepening LAB cause the gravity anomalies to begin increasing again toward the shelf edge. We propose that the  $\sim 20$  mGal gravity anomaly confirm the existence of the subparallel rift segments, and thus, postulate that a localized rift might have triggered a focal deformation process that gave rise to the LACZ, as discussed further in section 5.3.2.

The predicted trajectory of the Great Meteor hot spot is parallel to the New England Seamounts chain and cross-cuts the two rifting segments (Figure 9a) along its ocean-to-continent path, where numerous igneous intrusions are present [Crough, 1981; Selway, 2014]. Along the hot spot track, released heat could have weakened or thermally altered the lithosphere [Morgan, 1983].

### 5.3. Conceptual Models

To unfold the mechanism that gave rise to the presence of the LACZ and the lithospheric thinning, we interpret the preferred conductivity model in conjunction with the regional shear-wave velocity, gravity anomalies, and geological features. Based on this joint interpretation, we propose two conceptual models that are geologically plausible and may explain the underlying cause for the thinning of the lithosphere at the model center, and the enhancement of conductivity in the LACZ.



**Figure 9.** Regional gravity map compared with the preferred conductivity model. (a) New England gravity map: gray triangles represent the positions of the MT stations (from w14 in NNW to w3 in SSE), black rectangle denotes the positive gravity anomaly, and the dashed lines represent the rifted crust segments. The purple line denotes the predicted track of the Great Meteor hot spot, as described by Crough [1981]. (b) The green line indicates the gravity anomalies along the MT linear array. The brown line denotes the seafloor bathymetry. (c) The preferred conductivity model. White dashed line represents the depth varying LAB. The area bounded by the gray dashed line denotes a vertically extending conductor, possibly resulting from rift-derived sediments infill. The rectangle in Figures 9a and 9b indicates the location of the ~20 mGal gravity anomaly that coincides with the NNW upper LACZ, as seen beneath MT stations w13, s2, w11, and s3.

### 5.3.1. Kimberlite Intrusions

For the first conceptual model, we suggest the following scenario: lithospheric piercing by Kimberlite intrusions sourced from the New England Great Meteor hot spots. These magmatic intrusions propagated NW along the hot spot trajectory toward the continent. Further North along the Great Meteor hot spot track, numerous kimberlitic melts have intruded the Canadian Slave Craton from deep within the lithosphere to the surface, over the last ~500 Ma [Selway, 2014]. An MT study performed at the Grenville Province in southern Ontario, Canada, identified a conductive anomaly in the lower lithosphere that is spatially associated with low seismic velocities [Adetunji *et al.*, 2015]. This conductive anomaly is attributed to lithospheric refertilization by fluids associated with kimberlite fields magmatism. Additionally, a subvertical conductor located ~50 km along strike from the Mesozoic Kirkland Lake and Cobalt kimberlite fields is interpreted as refertilization of an old mantle scar [Adetunji *et al.*, 2014, 2015]. Thus, there is substantial evidence for kimberlite intrusions at the proximity of our study region.

Kimberlites are moderately electrically conductive (250–1100 Ωm) in comparison to continental host rocks, particularly when the kimberlite conductive elements form a continuous interlinked network [Kamara, 1981; Katsube and Kjarsgaard, 1996]. Since the direction of the Great Meteor hot spot track is only about 90 km NE to the location of our MT profile (Figure 9a), we postulate that hot spot melt swells contributed to a paleo thermal erosion and weakening in the lithosphere. Thus, these melts possibly enabled the intrusion of conductive kimberlitic rocks, as illustrated in Figure 10a. The kimberlite intrusions are hypothesized to be subparallel to the hot spot track due to the tendency of melt to be channeled into parallel rift zones of weakness, and thus, aligning between the bounding rift segments. To date, no surface expression of

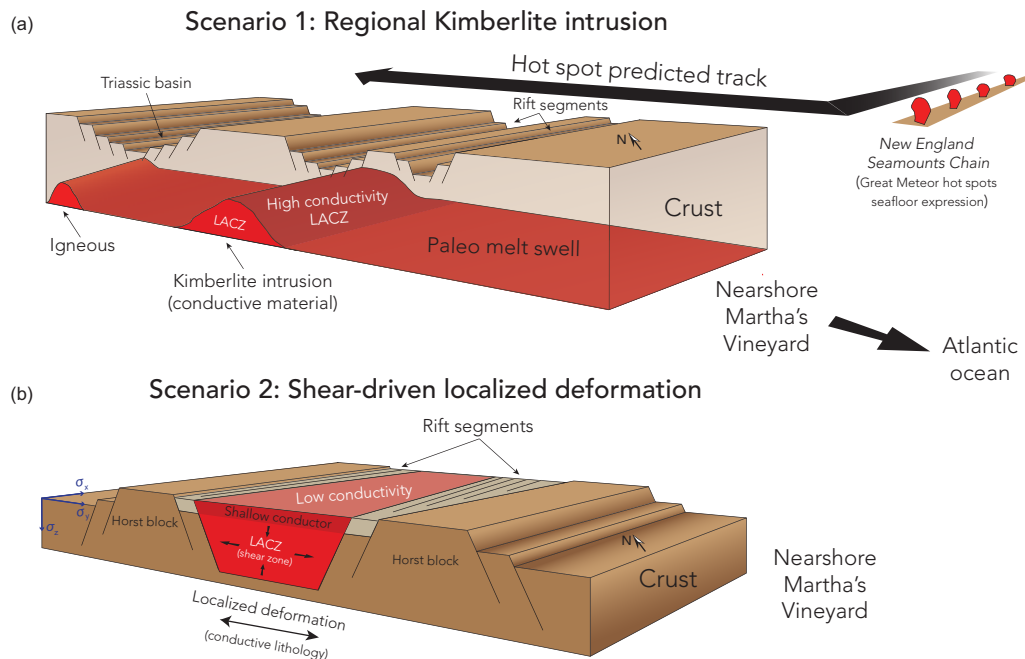


**Figure 10.** Conceptual models illustrating possible scenarios that could explain the presence of the anomalous conductive structure within the lithosphere. Red shades represent conductive areas. (a) A regional scale model showing kimberlite magmatic intrusions. (b) A local scale model showing structural deformation as a result of shearing. The conductivity axes orientation is denoted by the blue errors. This scenario accounts for the observed electrical anisotropy.

kimberlites was documented at the immediate vicinity of the MT profile. To the north of our study area, Menke *et al.* [2016] see a low velocity region in the upper-mantle that they postulate is the result of small-scale asthenospheric upwelling. Thus, if the asthenospheric upwelling extended southward along the New England continental margin, it might have enhanced the thermal erosion and weakening of the lithosphere beneath the MT profile, raising the electrical conductivity in the upper mantle. Although the southern edge of the observed velocity anomaly appears to extend to the south of the island of Martha's Vineyard, we do not see evidence for a generally raised conductivity in the asthenosphere, and so our profile constrains the southernmost extent of the anomalous region. We propose that a paleo-intrusion of kimberlites may explain the observed LACZ (Figures 6e and 10a). Apart from the thermal erosion hypothesis, alternative processes such as mantle scar refertilization [Adetunji *et al.*, 2014, 2015] or enrichment of the lithospheric keel by plume material [VanDecar *et al.*, 1995] might also explain the presence of the LACZ.

### 5.3.2. Shear-Driven Deformation

For our second conceptual model, we hypothesize that the LACZ results from shear-driven localized deformation. We suggest that the localized deformation resulting from rifting, enabled the emergence of the LACZ between two rift segments, as illustrated in Figure 10b. An MT study conducted at the north-central US along the Mid-Continent Rift system, suggests two elongate lower crustal suture-related conductive anomalies [Yang *et al.*, 2015]. These conductive anomalies were initially introduced during ancient rifting events and subsequently thrust deep into the lower crust and uppermost mantle. Yang *et al.* [2015] proposed that such conductive anomalies can serve as stable, long-lived markers, providing valuable constraints on deep structures ancient processes. Hence, we infer that in our region of study, such rift associated conductive anomalies are represented by the LACZ. A model by Eaton and Frederiksen [2007] suggests that deformation occurred along the Great Meteor hot spot track in eastern North America, due to shear in the lithospheric mantle keel arising from viscous coupling with the asthenospheric flow beneath.

Pommier *et al.* [2015] laboratory results indicate that some enhancement in conductivity can be achieved by shearing olivine. If melt is present during rifting then melt crystallization fabrics at shear-driven localized deformation fronts may significantly alter the lithosphere and upper mantle rheology [e.g., Holtzman and Kendall, 2010; Karato, 2012; Höink *et al.*, 2012; Soustelle *et al.*, 2014]. Experimental studies suggest that electrical conductivities are  $\sim 10$  times greater along the shear plane than perpendicular to it [Pommier *et al.*,

2015]. These studies agree well with our anisotropic modeling, which shows higher conductivities in the direction parallel to the MT profile. This observation, as well as the general increase in conductivity in region of likely shearing, (Figures 10b and 7), strongly suggests that rift associated deformation via lithospheric shearing is the cause of the observed LACZ.

To determine which of the proposed conceptual models describe a more plausible geological scenario, an MT study with a 3-D grid coverage is required. If kimberlite intrusion along the path of the hot spot track is episodic (consistent with the spacing of seamounts in the New England seamount chain), then both models would predict an LACZ oriented parallel to the rift structures (Figure 10). However, we would not expect the kimberlites to extend for great distances along strike from their point of intrusion, so in this case, the spatial extent of the conductor would be limited.

## 6. Conclusions

This paper presents the first conductivity model beneath the eastern North American continental margin, using two different magnetotelluric 2-D inversion methods. The applied smooth and hypothesis testing MT inversion models enabled us to produce a well-constrained model that was interpreted in conjunction with shear-wave velocity,  $P_s$  receiver function, gravity data and regional geological features. From our rigorous test models and joint interpretation, we conclude the following: (1) the LAB topography varies from 145 km at the NNW part of the model to 85 km at the model center (asthenospheric rise), then deepens back to 130 km at SSE (LAB averaged depth = 115 km); (2) a lithospheric thinning is represented by a  $\sim 350 \Omega\text{m}$  LACZ that extends vertically through the entire lithosphere; (3) at the LACZ, the conductivity parallel to the MT profile is enhanced relative to the geoelectric strike and bounding rifts segments.

We propose that the LACZ indicates the presence of a thinned lithosphere, which may have been caused by kimberlite intrusion or by alterations in lithology due to the regional structural shearing, occurred along the eastern North America continental passive margin during the Early Jurassic.

## Acknowledgments

This work was support by NSF grants OCE-0958878, OCE-1459035, OCE-1458392, and OCE-1536161 and WHOI Access to the Sea funds. Attias received funds to visit WHOI through the Woods Hole Exchange Programme administered by the University of Southampton Graduate School of the National Oceanography Centre, Southampton. We thank Matthew Gould, Chris Judge and John Bailey (WHOI); Chris Armerding, Jacques Lemire, Jacob Perez, and John Souder (Scripps) for assisting with the instrumentation and survey cruises. Additionally, we thank Nicholas Harmon, Matthew R. Agius, Dan Bassett, Timothy A. Minshull, and Catherine Rychnert for useful discussions. We gratefully acknowledge the captain and scientific party of the R/V Marcus G. Langseth. Finally, we thank reviewers Marion Jegen and Ian Ferguson for their constructive suggestions that improved this manuscript.

## References

- Abt, D. L., K. M. Fischer, S. W. French, H. A. Ford, H. Yuan, and B. Romanowicz (2010), North American lithospheric discontinuity structure imaged by Ps and Sp receiver functions, *J. Geophys. Res.*, 115, B09301, doi:10.1029/2009JB006914.
- Adetunji, A. Q., I. J. Ferguson, and A. G. Jones (2014), Crustal and lithospheric scale structures of the Precambrian Superior-Grenville margin, *Tectonophysics*, 614, 146–169.
- Adetunji, A. Q., I. J. Ferguson, and A. G. Jones (2015), Imaging the mantle lithosphere of the Precambrian Grenville Province: Large-scale electrical resistivity structures, *Geophys. J. Int.*, 201(2), 1040–1061.
- Artemieva, I. M. (2009), The continental lithosphere: Reconciling thermal, seismic, and petrologic data, *Lithos*, 109(1), 23–46.
- Auer, L., L. Boschi, T. Becker, T. Nissen-Meyer, and D. Giardini (2014), Savani: A variable resolution whole-mantle model of anisotropic shear velocity variations based on multiple data sets, *J. Geophys. Res.*, 119, 3006–3034, doi:10.1002/2013JB010773.
- Austin, J. A., P. L. Stoffa, J. D. Phillips, J. Oh, D. S. Sawyer, G. M. Purdy, E. Reiter, and J. Makris (1990), Crustal structure of the Southeast Georgia embayment-carolina trough: Preliminary results of a composite seismic image of a continental suture (?) and a volcanic passive margin, *Geology*, 18(10), 1023–1027.
- Baba, K., A. D. Chave, R. L. Evans, G. Hirth, and R. L. Mackie (2006), Mantle dynamics beneath the East Pacific Rise at 17°S: Insights from the Mantle Electromagnetic and Tomography (MELT) experiment, *J. Geophys. Res.*, 111, B02101, doi:10.1029/2004JB003598.
- Baba, K., N. Tada, L. Zhang, P. Liang, H. Shimizu, and H. Utada (2013), Is the electrical conductivity of the northwestern Pacific upper mantle normal?, *Geochem. Geophys. Geosyst.*, 14, 4969–4979, doi:10.1002/2013GC004997.
- Bassett, D., and A. B. Watts (2015), Gravity anomalies, crustal structure, and seismicity at subduction zones: 1. Seafloor roughness and subducting relief, *Geochem. Geophys. Geosyst.*, 16, 1508–1540, doi:10.1002/2014GC005684.
- Bédard, J. H. (1985), The opening of the Atlantic, the mesozoic New England igneous province, and mechanisms of continental breakup, *Tectonophysics*, 113(3), 209–232.
- Benson, R. N., and R. G. Doyle (1988), Early mesozoic rift basins and the development of the United States middle Atlantic continental margin, in *Triassic-Jurassic Rifting, Continental Breakup and the Origin of the Atlantic Ocean Passive Margins, Part A*, edited by W. Manspeizer, pp. 99–127, Elsevier, New York.
- Berdichevsky, M. N., and V. I. Dmitriev (2008), *Models and Methods of Magnetotellurics*, Springer, Berlin.
- Booker, J. R. (2014), The magnetotelluric phase tensor: A critical review, *Surv. Geophys.*, 35(1), 7–40.
- Caldwell, T. G., H. M. Bibby, and C. Brown (2004), The magnetotelluric phase tensor, *Geophys. J. Int.*, 158(2), 457–469.
- Cammarano, F., and B. Romanowicz (2007), Insights into the nature of the transition zone from physically constrained inversion of long-period seismic data, *Proc. Natl. Acad. Sci., U. S. A.*, 104(22), 9139–9144.
- Cande, S. C., J. M. Stock, R. D. Müller, and T. Ishihara (2000), Cenozoic motion between east and west Antarctica, *Nature*, 404(6774), 145–150.
- Chave, A. D., and D. J. Thomson (2003), A bounded influence regression estimator based on the statistics of the hat matrix, *J. R. Stat. Soc., Ser. C*, 52(3), 307–322.
- Chave, A. D., and D. J. Thomson (2004), Bounded influence magnetotelluric response function estimation, *Geophys. J. Int.*, 157(3), 988–1006.

- Chu, R., W. Leng, D. V. Helmberger, and M. Gurnis (2013), Hidden hotspot track beneath the eastern United States, *Nat. Geosci.*, 6(11), 963–966.
- Constable, S. C., R. L. Parker, and C. G. Constable (1987), Occam's inversion: A practical algorithm for generating smooth models from electromagnetic sounding data, *Geophysics*, 52(3), 289–300.
- Constable, S. C., A. S. Orange, G. M. Hoversten, and H. F. Morrison (1998), Marine magnetotellurics for petroleum exploration, Part I: A sea-floor equipment system, *Geophysics*, 63(3), 816–825.
- Cox, C. S. (1981), On the electrical conductivity of the oceanic lithosphere, *Phys. Earth Planet. Inter.*, 25(3), 196–201.
- Cox, C., S. Constable, A. Chave, and S. Webb (1986), Controlled-source electromagnetic sounding of the oceanic lithosphere, *Nature*, 320, 52–54.
- Crough, S. T. (1981), Mesozoic hotspot epeirogeny in eastern North America, *Geology*, 9(1), 2–6.
- Crough, S. T., W. J. Morgan, and R. B. Hargraves (1980), Kimberlites: Their relation to mantle hotspots, *Earth Planet. Sci. Lett.*, 50(1), 260–274.
- Dalton, C. A., G. Ekström, and A. M. Dziewonski (2009), Global seismological shear velocity and attenuation: A comparison with experimental observations, *Earth Planet. Sci. Lett.*, 284(1), 65–75.
- de Voogd, B., C. E. Keen, and W. A. Kay (1990), Fault reactivation during Mesozoic extension in eastern offshore Canada, *Tectonophysics*, 173(1), 567–580.
- deGroot Hedlin, C., and S. Constable (1990), Occam's inversion to generate smooth, two-dimensional models from magnetotelluric data, *Geophysics*, 55(12), 1613–1624.
- Deschamps, F., S. Lebedev, T. Meier, and J. Trampert (2008), Stratified seismic anisotropy reveals past and present deformation beneath the East-central United States, *Earth Planet. Sci. Lett.*, 274(3), 489–498.
- Duncan, R. A. (1984), Age progressive volcanism in the New England seamounts and the opening of the central Atlantic Ocean, *J. Geophys. Res.*, 89, 9980–9990.
- Dunning, G., and J. Hodych (1990), U-Pb zircon and baddeleyite age for the Palisade and Gettysburg sills of northeast United States: Implications for the age of the Triassic-Jurassic boundary, *Geology*, 18, 795–798.
- Eaton, D. W., and A. Frederiksen (2007), Seismic evidence for convection-driven motion of the North American plate, *Nature*, 446(7134), 428–431.
- Eaton, D. W., F. Derbyshire, R. L. Evans, H. Grüter, A. G. Jones, and X. Yuan (2009), The elusive lithosphere–asthenosphere boundary (LAB) beneath cratons, *Lithos*, 109(1), 1–22.
- Egbert, G. D. (1997), Robust multiple-station magnetotelluric data processing, *Geophys. J. Int.*, 130(2), 475–496.
- Evans, R. (2012), Chapter 3: Earths electromagnetic environment. Part 1: Conductivity of earth materials, in *The Magnetotelluric Method: Theory and Practice*, edited by A. D. Chave and A. G. Jones, 50 pp., Cambridge Univ. Press, New York, ISBN: 9780521819275.
- Evans, R., et al. (1999), Asymmetric electrical structure in the mantle beneath the East Pacific Rise at 17°S, *Science*, 286(5440), 752–756.
- Evans, R. L., G. Hirth, K. Baba, D. Forsyth, A. Chave, and R. Mackie (2005), Geophysical evidence from the MELT area for compositional controls on oceanic plates, *Nature*, 437(7056), 249–252.
- Fischer, K. M., H. A. Ford, D. L. Abt, and C. A. Rychert (2010), The lithosphere–asthenosphere boundary, *Annu. Rev. Earth Planet. Sci.*, 38, 551–575.
- French, S., and B. Romanowicz (2014), Whole-mantle radially anisotropic shear velocity structure from spectral-element waveform tomography, *Geophys. J. Int.*, 199(3), 1303–1327.
- French, S., V. Lekic, and B. Romanowicz (2013), Waveform tomography reveals channeled flow at the base of the oceanic asthenosphere, *Science*, 342(6155), 227–230.
- Fullea, J., M. Muller, and A. Jones (2011), Electrical conductivity of continental lithospheric mantle from integrated geophysical and petrological modeling: Application to the Kaapvaal Craton and Rehoboth Terrane, southern Africa, *J. Geophys. Res.*, 116, B10202, doi:10.1029/2011JB008544.
- Hames, W., P. Renne, and C. Ruppel (2000), New evidence for geologically instantaneous emplacement of earliest Jurassic Central Atlantic magmatic province basalts on the North American margin, *Geology*, 28(9), 859–862.
- Hammond, W. C., and E. D. Humphreys (2000), Upper mantle seismic wave velocity: Effects of realistic partial melt geometries, *J. Geophys. Res.*, 105, 10,975–10,986.
- Hansen, S. E., A. A. Nyblade, J. Julià, P. H. Dirks, and R. J. Durrheim (2009), Upper-mantle low-velocity zone structure beneath the Kaapvaal craton from S-wave receiver functions, *Geophys. J. Int.*, 178(2), 1021–1027.
- Heaman, L., and B. Kjarsgaard (2000), Timing of eastern north American kimberlite magmatism: Continental extension of the Great Meteor hotspot track?, *Earth Planet. Sci. Lett.*, 178(3), 253–268.
- Höink, T., A. Lenardic, and M. Richards (2012), Depth-dependent viscosity and mantle stress amplification: Implications for the role of the asthenosphere in maintaining plate tectonics, *Geophys. J. Int.*, 191(1), 30–41.
- Holbrook, W. S., and P. B. Kelemen (1993), Large igneous province on the US Atlantic margin and implications for magmatism during continental breakup, *Nature*, 364, 433–436.
- Holbrook, W. S., E. Reiter, G. Purdy, D. Sawyer, P. Stoffa, J. Austin, J. Oh, and J. Makris (1994), Deep structure of the US Atlantic continental margin, offshore South Carolina, from coincident ocean bottom and multichannel seismic data, *J. Geophys. Res.*, 99, 9155–9178.
- Holtzman, B. K., and J. Kendall (2010), Organized melt, seismic anisotropy, and plate boundary lubrication, *Geochim. Geophys. Geosyst.*, 11, Q0AB06, doi:10.1029/2010GC003296.
- Hutchinson, D. R., K. D. Kitgord, and R. S. Detrick (1986), Rift basins of the long island platform, *GSA Bull.*, 97(6), 688–702.
- Jones, A. G. (2012), Distortion of magnetotelluric data: Its identification and removal, in *The Magnetotelluric Method: Theory and Practice*, edited by A. D. Chave, 219 pp., Cambridge University Press, Cambridge, U. K.
- Jones, A. G., S. Fishwick, R. L. Evans, M. R. Muller, and J. Fullea (2013), Velocity-conductivity relations for cratonic lithosphere and their application: Example of Southern Africa, *Geochim. Geophys. Geosyst.*, 14, 806–827, doi:10.1002/ggge.20075.
- Kamara, A. (1981), Review: Geophysical methods for kimberlite prospecting, *Explor. Geophys.*, 12(3), 43–51.
- Kapinos, G., U. Weckmann, M. Jegen-Kulcsar, N. Meqbel, A. Neska, T. Katjiuongua, S. Hoelz, and O. Ritter (2016), Electrical resistivity image of the South Atlantic continental margin derived from onshore and offshore magnetotelluric data, *Geophys. Res. Lett.*, 43, 154–160, doi:10.1002/2015GL066811.
- Karato, S.-i. (2012), On the origin of the asthenosphere, *Earth Planet. Sci. Lett.*, 321, 95–103.
- Katsube, T., and B. Kjarsgaard (1996), Physical property characteristics of Canadian Kimberlites in Searching for diamond in Canada, *Geol. Surv. Canada*, 3228, 241–242.
- Kawakatsu, H., P. Kumar, Y. Takei, M. Shinohara, T. Kanazawa, E. Araki, and K. Suyehiro (2009), Seismic evidence for sharp lithosphere–asthenosphere boundaries of oceanic plates, *Science*, 324(5926), 499–502.

- Kelemen, P. B., and W. S. Holbrook (1995), Origin of thick, high-velocity igneous crust along the US east Coast Margin, *J. Geophys. Res.*, **100**, 10,077–10,094.
- Key, K. (2016), MARE2DEM: A 2-D inversion code for controlled-source electromagnetic and magnetotelluric data, *Geophys. J. Int.*, **207**(1), 571–588.
- Key, K., and J. Ovall (2011), A parallel goal-oriented adaptive finite element method for 2.5-D electromagnetic modelling, *Geophys. J. Int.*, **186**(1), 137–154.
- Key, K., S. Constable, L. Liu, and A. Pommier (2013), Electrical image of passive mantle upwelling beneath the northern East Pacific Rise, *Nature*, **495**(7442), 499–502.
- Kjarsgaard, B. (2007), Kimberlite pipe models: Significance to exploration, in *Proceedings of Exploration*, vol. 7, edited by B. Milkereit, pp. 667–677., Exploration in the New Millennium, Toronto, Ontario, Canada.
- Kumar, P., et al. (2005), The lithosphere-asthenosphere boundary in the North-West Atlantic region, *Earth Planet. Sci. Lett.*, **236**(1), 249–257.
- Kustowski, B., G. Ekström, and A. Dziewoński (2008), Anisotropic shear-wave velocity structure of the Earth's mantle: A global model, *J. Geophys. Res.*, **113**, B06306, doi:10.1029/2007JB005169.
- Laxon, S., and D. McAdoo (1994), Arctic Ocean gravity field derived from ERS-1 satellite altimetry, *Science*, **265**(5172), 621–624.
- Lebedev, S., and R. D. Van Der Hilst (2008), Global upper-mantle tomography with the automated multimode inversion of surface and S-wave forms, *Geophys. J. Int.*, **173**(2), 505–518.
- Levin, V., W. Menke, and J. Park (2000), No regional anisotropic domains in the northeastern US Appalachians, *J. Geophys. Res.*, **105**, 19,029–19,042.
- Li, X., R. Kind, X. Yuan, I. Wölbern, and W. Hanka (2004), Rejuvenation of the lithosphere by the Hawaiian plume, *Nature*, **427**(6977), 827–829.
- Li, X., X. Yuan, and R. Kind (2007), The lithosphere-asthenosphere boundary beneath the western United States, *Geophys. J. Int.*, **170**(2), 700–710.
- Lizarralde, D., A. Chave, G. Hirth, and A. Schultz (1995), Northeastern Pacific mantle conductivity profile from long-period magnetotelluric sounding using Hawaii-to-California submarine cable data, *J. Geophys. Res.*, **100**, 17,837–17,854.
- MacGregor, L., M. Sinha, and S. Constable (2001), Electrical resistivity structure of the Valu Fa ridge, Lau Basin, from marine controlled-source electromagnetic sounding, *Geophys. J. Int.*, **146**(1), 217–236.
- Malinconico, M. (2003), Paleo-maximum thermal structure of the Triassic Taylorsville (Virginia) basin: Evidence for border fault convection and implications for duration of syn-rift sedimentation and long-term elevated heat flow, in *The Great Rift Valleys of Pangea in Eastern North America, Tectonics, Structure, and Volcanism*, edited by P. M. LeTourneau and P. E. Olsen, vol. 1, pp. 80–103., Columbia University Press, New York.
- Manspeizer, W., and H. L. Cousminer (1988), Late Triassic-Early Jurassic synrift basins of the US Atlantic margin, *Geol. North Am.*, **2**, 197–216.
- Marzoli, A., P. R. Renne, E. M. Piccirillo, M. Ernesto, G. Bellieni, and A. De Min (1999), Extensive 200-million-year-old continental flood basalts of the Central Atlantic Magmatic Province, *Science*, **284**(5414), 616–618.
- McAdoo, D., and S. Laxon (1997), Antarctic tectonics: Constraints from an ers-1 satellite marine gravity field, *Science*, **276**(5312), 556–561.
- McAlpine, K. (1990), *Mesozoic Stratigraphy, Sedimentary Evolution, and Petroleum Potential of the Jeanne D'Arc Basin, Grand Banks of New Foundland*, vol. 89, Geolo. Surv. of Canada, Alberta, Canada.
- McHone, J. G. (1996), Broad-terrane Jurassic flood basalts across northeastern North America, *Geology*, **24**(4), 319–322.
- McHone, J. G. (2000), Non-plume magmatism and rifting during the opening of the central Atlantic Ocean, *Tectonophysics*, **316**(3), 287–296.
- McHone, J. G., and J. R. Butler (1984), Mesozoic igneous provinces of New England and the opening of the North Atlantic Ocean, *Geol. Soc. Am. Bull.*, **95**(7), 757–765.
- Menke, W., P. Skryzalin, V. Levin, T. Harper, F. Darbyshire, and T. Dong (2016), The Northern Appalachian Anomaly: A modern asthenospheric upwelling, *Geophys. Res. Lett.*, **43**, 10,173–10,179, doi:10.1002/2016GL070918.
- Mohsen, A., R. Kind, S. V. Sobolev, M. Weber, and DESERT Group (2006), Thickness of the lithosphere east of the Dead Sea transform, *Geophys. J. Int.*, **167**(2), 845–852.
- Morgan, W. J. (1981), Hotspot tracks and the opening of the Atlantic and Indian oceans, *Oceanic Lithosphere*, **7**, 443–487.
- Morgan, W. J. (1983), Hotspot tracks and the early rifting of the Atlantic, *Tectonophysics*, **94**(1–4), 123–139.
- Naif, S., K. Key, S. Constable, and R. Evans (2013), Melt-rich channel observed at the lithosphere-asthenosphere boundary, *Nature*, **495**(7441), 356–359.
- Olsen, P., R. Schlische, and P. Gore (1989), Tectonic, depositional, and paleoecological history of Early Mesozoic Rift Basins, Eastern North America, in *28th International Geological Congress Field Trip, T351*, edited by P. E. Olsen, R. W. Schlische, and P. J. W. Core, 174 pp., American Geophysical Union, Washington, D. C.
- Olsen, P. E., D. V. Kent, B. Cornet, W. K. Witte, and R. W. Schlische (1996), High-resolution stratigraphy of the Newark rift basin (early Mesozoic, eastern North America), *Geol. Soc. Am. Bull.*, **108**(1), 40–77.
- Poag, C. W. (1978), Stratigraphy of the Atlantic continental shelf and slope of the United States, *Annu. Rev. Earth Planet. Sci.*, **6**, 251–280.
- Pollitz, F. F., and W. D. Mooney (2016), Seismic velocity structure of the crust and shallow mantle of the Central and Eastern United States by seismic surface wave imaging, *Geophys. Res. Lett.*, **43**, 118–126, doi:10.1002/2015GL066637.
- Pommier, A., K. Leinenweber, D. L. Kohlstedt, C. Qi, E. J. Garnero, S. J. Mackwell, and J. A. Tyburczy (2015), Experimental constraints on the electrical anisotropy of the lithosphere-asthenosphere system, *Nature*, **522**(7555), 202–206.
- Ratcliffe, N., and W. Burton (1985), Fault reactivation models for origin of the Newark basin and studies related to eastern US seismicity, in *Proceedings of the Second US Geological Survey Workshop on the Early Mesozoic Basins of the Eastern United States, U.S. Geol. Surv. Circ.*, **946**, edited by G. R. Robinson and A. I. Froelich, pp. 36–45, U.S. Geol. Surv., Reston, Va.
- Ritsema, J., A. Deuss, H. Van Heijst, and J. Woodhouse (2011), S40RTS: A degree-40 shear-velocity model for the mantle from new Rayleigh wave dispersion, teleseismic traveltime and normal-mode splitting function measurements, *Geophys. J. Int.*, **184**(3), 1223–1236.
- Rodi, W., and R. L. Mackie (2001), Nonlinear conjugate gradients algorithm for 2-D magnetotelluric inversion, *Geophysics*, **66**(1), 174–187.
- Romanowicz, B. (2009), The thickness of tectonic plates, *Science*, **324**(5926), 474–476.
- Rondenay, S., K. Spieker, L. Sawade, F. Halpaap, and M. Farestveit (2017), GLImER—A new global database of teleseismic receiver functions for imaging earth structure, *Seismol. Res. Lett.*, **88**(1), 1–10.
- Rychert, C. A., and P. M. Shearer (2009), A global view of the lithosphere-asthenosphere boundary, *Science*, **324**(5926), 495–498.
- Rychert, C. A., K. M. Fischer, and S. Rondenay (2005), A sharp lithosphere-asthenosphere boundary imaged beneath eastern North America, *Nature*, **436**(7050), 542–545.

- Rychert, C. A., S. Rondenay, and K. M. Fischer (2007), P-to-Sand S-to-P imaging of a sharp lithosphere-asthenosphere boundary beneath eastern North America, *J. Geophys. Res.*, 112, B08314, doi:10.1029/2006JB004619.
- Sandwell, D. T., R. D. Müller, W. H. Smith, E. Garcia, and R. Francis (2014), New global marine gravity model from CryoSat-2 and Jason-1 reveals buried tectonic structure, *Science*, 346(6205), 65–67.
- Sarafian, E., R. Evans, J. A. Collins, J. Elsenbeck, G. A. Gaetani, J. B. Gaherty, G. Hirth, and D. Lizarralde (2015), The electrical structure of the central Pacific upper mantle constrained by the NoMelt experiment, *Geochem. Geophys. Geosyst.*, 16, 1115–1132, doi:10.1002/2014GC005709.
- Schaeffer, A., and S. Lebedev (2013), Global shear speed structure of the upper mantle and transition zone, *Geophys. J. Int.*, 207(3), 1739–1766, doi:10.1029/2009JB007078.
- Schaeffer, A., and S. Lebedev (2014), Imaging the North American continent using waveform inversion of global and USArray data, *Earth Planet. Sci. Lett.*, 402, 26–41.
- Schlee, J., J. C. Behrendt, J. A. Grow, J. M. Robb, R. E. Mattick, P. Taylor, and B. J. Lawson (1976), Regional geologic framework off northeastern United States, *AAPG Bull.*, 60(6), 926–951.
- Schmandt, B., and F.-C. Lin (2014), P and S wave tomography of the mantle beneath the United States, *Geophys. Res. Lett.*, 41, 6342–6349, doi:10.1002/2014GL061231.
- Schwalenberg, K., V. Rath, and V. Haak (2002), Sensitivity studies applied to a two-dimensional resistivity model from the central Andes, *Geophys. J. Int.*, 150(3), 673–686.
- Selway, K. (2014), On the causes of electrical conductivity anomalies in tectonically stable lithosphere, *Surv. Geophys.*, 35(1), 219–257.
- Sheridan, R. E., D. L. Musser, L. Glover, M. Talwani, J. I. Ewing, W. S. Holbrook, G. M. Purdy, R. Hawman, and S. Smithson (1993), Deep seismic reflection data of EDGE US mid-Atlantic continental-margin experiment: Implications for Appalachian sutures and Mesozoic rifting and magmatic underplating, *Geology*, 21(6), 563–567.
- Siegel, J., M. Person, B. Dugan, D. Cohen, D. Lizarralde, and C. Gable (2014), Influence of late Pleistocene glaciations on the hydrogeology of the continental shelf offshore Massachusetts, USA, *Geochem. Geophys. Geosyst.*, 15, 4651–4670, doi:10.1002/2014GC005569.
- Singh, R., Y. Kant, and L. Vanyan (1995), Deep electrical conductivity structure beneath the southern part of the Indo-Gangetic plains, *Phys. Earth Planet. Int.*, 88(3), 273–283.
- Sleep, N. H. (1990), Monteregian hotspot track: Along-lived mantle plume, *J. Geophys. Res.*, 95, 21,983–21,990.
- Snyder, D. B. (2008), Stacked uppermost mantle layers within the slave craton of NW Canada as defined by anisotropic seismic discontinuities, *Tectonics*, 27, TC4006, doi:10.1029/2007TC002132.
- Soustelle, V., N. P. Walte, M. G. M. Manthilake, and D. J. Frost (2014), Melt migration and melt-rock reactions in the deforming Earth's upper mantle: Experiments at high pressure and temperature, *Geology*, 42(1), 83–86.
- Steckler, M. S., G. S. Mountain, K. G. Miller, and N. Christie-Blick (1999), Reconstruction of Tertiary progradation and clinoform development on the New Jersey passive margin by 2-D backstripping, *Mar. Geol.*, 154(1), 399–420.
- Torsvik, T. H., K. Burke, B. Steinberger, S. J. Webb, and L. D. Ashwal (2010), Diamonds sampled by plumes from the core-mantle boundary, *Nature*, 466(7304), 352–355.
- Tseng, H. Y., T. Onstott, R. Burruss, and D. Miller (1996), Constraints on the thermal history of Taylorsville Basin, Virginia, USA, from fluid-inclusion and fission-track analyses: implications for subsurface geomicrobiology experiments, *Chem. Geol.*, 127(4), 297–311.
- VanDecar, J. C., D. E. James, and M. Assumpção (1995), Seismic evidence for a fossil mantle plume beneath South America and implications for plate driving forces, *Nature*, 378(6552), 25–31.
- Vozar, J., A. G. Jones, J. Fullea, M. R. Agius, S. Lebedev, F. Le Pape, and W. Wei (2014), Integrated geophysical-petrological modeling of lithosphere-asthenosphere boundary in central Tibet using electromagnetic and seismic data, *Geochem. Geophys. Geosyst.*, 15, 3965–3988, doi:10.1002/2014GC005365.
- Wannamaker, P. E., A. D. Chave, J. R. Booker, A. G. Jones, J. H. Filloux, Y. Ogawa, M. Unsworth, P. Tarits, and R. Evans (1996), Magnetotelluric experiment probes deep physical state of southeastern United States, *EOS*, 77(34), 329–333.
- Welsink, H., J. Dwyer, and R. Knight (1989), Tectono-stratigraphy of the passive margin off Nova Scotia, 46, 215–231.
- Wheelock, B., S. Constable, and K. Key (2015), The advantages of logarithmically scaled data for electromagnetic inversion, *Geophys. J. Int.*, 201(3), 1765–1780.
- Withjack, M. O., P. E. Olsen, and R. W. Schlische (1995), Tectonic evolution of the Fundy rift basin, Canada: Evidence of extension and shortening during passive margin development, *Tectonics*, 14, 390–405.
- Withjack, M. O., R. W. Schlische, and P. E. Olsen (1998), Diachronous rifting, drifting, and inversion on the passive margin of central eastern North America: An analog for other passive margins, *AAPG Bull.*, 82(5), 817–835.
- Wittlinger, G., and V. Farra (2007), Converted waves reveal a thick and layered tectosphere beneath the Kalahari super-craton, *Earth Planet. Sci. Lett.*, 254(3), 404–415.
- Worzewski, T., M. Jegen, H. Kopp, H. Brasse, and W. T. Castillo (2011), Magnetotelluric image of the fluid cycle in the Costa Rican subduction zone, *Nature Geosci.*, 4(2), 108–111.
- Wyer, P., and A. Watts (2006), Gravity anomalies and segmentation at the East Coast, USA continental margin, *Geophys. J. Int.*, 166(3), 1015–1038.
- Yang, B., G. D. Egbert, A. Kelbert, and N. M. Meqbel (2015), Three-dimensional electrical resistivity of the north-central USA from EarthScope long period magnetotelluric data, *Earth Planet. Sci. Lett.*, 422, 87–93.
- Yuan, H., S. French, P. Cupillard, and B. Romanowicz (2014), Lithospheric expression of geological units in central and eastern North America from full waveform tomography, *Earth Planet. Sci. Lett.*, 402, 176–186.